Title
Magnetometry and Imaging with Nitrogen Vacancy Centers in Diamond

Author
Lourette, Sean

Publication Date
2019

Peer reviewed|Thesis/dissertation

Magnetometry and Imaging with Nitrogen Vacancy Centers in Diamond

by

Sean Lourette

A dissertation submitted in partial satisfaction of the

requirements for the degree of

Doctor of Philosophy

in

Physics

in the

Graduate Division

of the

University of California, Berkeley

Committee in charge:

Professor Dmitry Budker, Chair
Professor Dan Stamper-Kurn
Professor Philip Marcus

Fall 2019

Magnetometry and Imaging with Nitrogen Vacancy Centers in Diamond

Abstract

Magnetometry and Imaging with Nitrogen Vacancy Centers in Diamond

by

Sean Lourette

Doctor of Philosophy in Physics

University of California, Berkeley

Professor Dmitry Budker, Chair

After a brief introduction to nitrogen vacancy (NV) centers and related physics, a description is presented of the principles and methodology of the diamond-based imaging magnetometer using an ensemble of NV centers. The diamond-based magnetic imaging platform is used to realize a force-induced remnant magnetization spectroscopy technique in which specific biomolecular binding is measured and detection is performed with wide-field optical and diamond-based magnetometry. This diamond-based technique that has both optical and magnetic detection modalities may be adapted for massively parallel screening of arrays of nanoscale samples. In a separate, but similarly inspired experiment, a description is given of the methods used to analyze the motion of a microscopic ferromagnetic particle levitated above a superconducting niobium surface.

To my parents

for their loving support and encouragement
throughout my entire life.

Contents

List of Figures

List of Tables

Acknowledgments

I would like to start out by thanking my dissertation chair, Dmitry Budker, for being an outstanding mentor and research advisor, and for sharing his contagious enthusiasm and passion for physics and research with me. Despite his seemingly impossible schedule and travel plans, he would somehow always find time meet with me on a moment's notice, whenever I needed his assistance or advice. It is clear to me that he does everything he can to ensure that his students will succeed, and for that I am extremely grateful.

I would also like to express my gratitude to Andrey Jarmola for introducing me to NV physics when I first joined the group, and continuing to be the person I turn to for guidance, when the NV centers did not want to cooperate.

I also want to thank Tao Wang and Metin Kayci for their contribution to our research projects, and for being a pleasure to work with, making my time here at Berkeley more enjoyable. Finally, I would like to share my appreciation for Lykourgos Bougas, Chris Hovde, Shoujun Xu, Huijie Zheng, and Romain Chainard for working with me on various projects throughout my degree.

Chapter 1

An Introduction to Diamond-Based Sensing with NV centers

In the broader context of Atomic Molecular and Optical (AMO) physics, diamond-based sensing is a relatively young field facing many challenges, uncertainties, and promising applications. It sits on the boundary between AMO and condensed matter physics, behaving like trapped atoms coupled to a lattice. Much in the way that impurities can be introduced into semiconductors, defects can be introduced into diamond in order to change the system into one with more desirable properties. In the following chapter, I will present a brief background and motivation for the use of diamond-based sensing with NV centers.

1.1 Diamond

Diamond is widely known both as the hardest naturally-occurring known material as well as a precious clear colorless jewel. Consisting entirely of carbon atoms, its crystalline structure, known as the diamond lattice, has a unit cell containing eight atoms where each atom has four equally-spaced nearest neighbors that form a regular tetrahedron [1]. While being an excellent heat conductor, diamond is a non-metal possessing a sizable band-gap of 5.5 eV between its valance and condition band, making it an electrical insulator [2]. Diamond is transparent to visible light, which is made up of photons ranging from 1.65 eV to 3.10 eV. Being transparent to visible light makes diamond an excellent material for sensory applications, allowing for optical access to defects of interest within its crystalline lattice.

Defects in diamond, if present in sufficiently high concentrations, will affect the hue of the diamond. It is for this reason diamond gemstones can be obtained in a wide variety of colors, and the defects responsible are commonly referred to as 'color centers'. These color centers have ground state and excited states whose energies have differences corresponding to the energy of a visible photon, and thus will absorb light of a particular wavelength, altering the hue of the diamond. The NV center is of particular interest, possessing many useful properties that will be discussed in the following section.

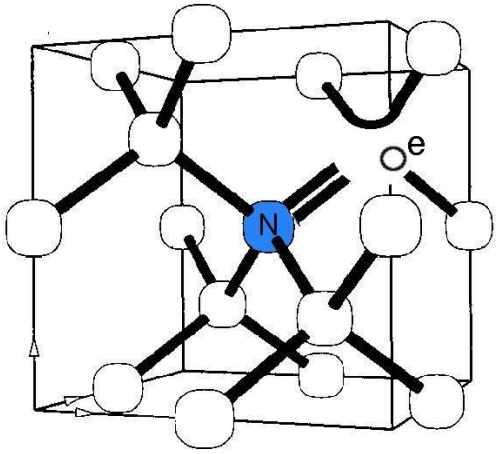

Figure 1.1: Structure of the NV center in diamond. Each atom in the lattice has four nearest neighbors, forming a regular tetrahedron. An NV center is a lattice defect consisting of a nitrogen atom adjacent to a vacancy. The NV center's six electrons can be seen surrounding the vacancy: two from the nitrogen, one from each carbon, and an extra donated form the lattice to give the NV its negative charge state. Reprinted from Wikipedia, by Materialscientist under CC BY-SA 3.0.

1.2 The NV center

The NV center is a particular point defect in diamond, in which a pair of neighboring carbon atoms have been replaced with a single nitrogen atom, occupying one of the two lattice sites. The other lattice site is left vacant and is referred to as a vacancy. Since each lattice site in diamond has four nearest neighbors, there are four different families of NV centers, each having its NV axis (line passing through the nitrogen and vacancy) aligned along a different orientation. The NV center is symmetric under 120° rotations about its axis, and thus possesses C_{3v} symmetry. This symmetry can be used to classify the 3 orbitals as E, A_1, and A_2 [3], which is analogous to how spherical symmetry results in the spherical harmonics and the s, p, d, and f orbitals of a hydrogen atom.

The NV center has two stable charge states: NV^0 and NV^-. Typically, when we talk about NV centers, we are referring specifically to the negative charge state, which is of great interest for reasons that will be discussed later in this section. The negatively charged NV center has six valance electrons surrounding the vacancy: two valance electrons of the nitrogen, one from each of the three adjacent carbon atoms, and one from an electron donor defect somewhere in the lattice (see Fig. 1.1). In the ground state configuration, the first four electrons fill the two orbitals of lowest energy, forming a closed shell. By Hund's rule, the remaining two electrons occupy the remaining two (degenerate) orbitals in such a way that maximizes the total spin, putting them into a symmetric $S = 1$ spin triplet state [4]. This ground-state electron configuration is known as $^3A_2$.

1.2.1 The Ground-State Hamiltonian

The ground state manifold, ($^3A_2$), has its 3-fold degeneracy lifted by the electron-electron spin interaction, favoring the antiparallel $\left(\frac{1}{\sqrt{2}}|\uparrow\downarrow\rangle + \frac{1}{\sqrt{2}}|\uparrow\downarrow\rangle\right)$ configuration over the two parallel ones ($|\uparrow\uparrow\rangle, |\downarrow\downarrow\rangle$). This energy splitting as known as the zero-field splitting (ZFS) and is written as $D = 2.87\,\text{GHz}$. The degeneracy is further lifted in the presence of electric and magnetic fields. The Hamiltonian governing these interactions can be written as follows:

$$\mathcal{H}_S = DS_z^2 + E\left(S_x^2 - S_y^2\right) + g_s\mu_B\vec{B}\cdot\vec{S}, \tag{1.1}$$

where g_s is the electron g-factor, μ_B is the Bohr magneton, $\vec{E}$ and $\vec{B}$ are the electric and magnetic fields, and the vector components of $\vec{S} = S_x\hat{x} + S_y\hat{y} + S_z\hat{z}$ are the x, y, and z spin matrices for a $S = 1$ spin system [5]. This Hamiltonian is sometimes referred to as the 'fine structure' term, analogous to the corrections to the atomic spectrum related to the electron spin, and corrections of similar size (ie. Lamb shift, Darwin term). The hyperfine structure refers to spectral splittings related to nuclear spin, I, and for NV centers, is written as

$$\mathcal{H}_I = A_\parallel S_z I_z + A_\perp\left(S_x I_x + S_y I_y\right) + PI_z^2 - g_I\mu_N\vec{B}\cdot\vec{I}, \tag{1.2}$$

where g_I is the nuclear g-factor, μ_N is the nuclear magneton, P is the nuclear quadrupole coupling $A_\parallel$ and $A_\perp$ are the axial and transverse hyperfine constants, and the vector components of $\vec{I} = I_x\hat{x} + I_y\hat{y} + I_z\hat{z}$ are x, y, and z spin matrices for the nuclear spin ($I = 1$ for ^{14}N, $I = 1/2$ for ^{15}N) [5].

1.2.2 Energy Levels and Optical Transitions

An energy level diagram of the NV center (negatively charged) is depicted in Fig. 1.2. The ground ($^3A_2$) and excited (^3E) triplet state manifolds are shown on the left, and the singlet states (^1E and $^1A_1$) are shown on the right. For NV centers, the optical transitions have $\Delta m_s = 0$ selection rules, and are therefore spin preserving. From the energy levels shown in Fig. 1.2, we can see that there are four optical transitions. The three optical transitions the couple the ground and excited (triplet) states have corresponding wavelengths of 637 nm.

However, unlike the other atomic systems such as trapped atoms or alkali-metal vapor cells whose atoms interact with a very narrow range of wavelength, the NV centers are coupled to a lattice and can therefore interact with photons of a large range of energies by converting the excess energy into phonic excitations of the lattice, which are dissipated as thermal energy. Stated simply, each of the energy levels on the energy level diagram has a phonic sideband with a continuum of states. As a result, NV centers will typically absorb light having wavelength less than 637 nm, and will typically emit light having wavelength greater than 637 nm. The absorption and fluorescence spectrum of the NV center is shown in figure Fig. 1.3b, along with a visual explanation of the Stokes and Anti-Stokes shifts in Fig. 1.3a.

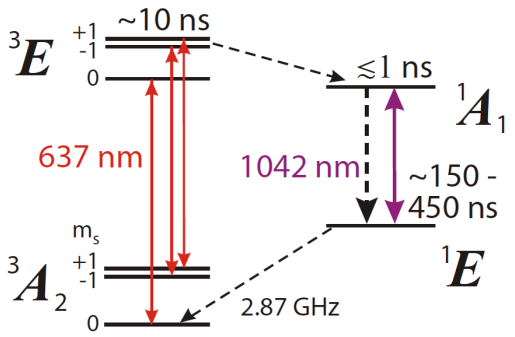

Figure 1.2: Energy levels of the NV center. Triplet states ($^3A_2$, ^3E) are positioned on the left, singlet states (^1E, $^1A_1$) are positioned on the right. Triplet substates are labelled by their spin projection, m_s. Excited states are labelled with their approximate lifetime. Solid arrows represent photon transitions, and dashed arrows represent non-radiative transitions. Reprint from [6], used with permission.

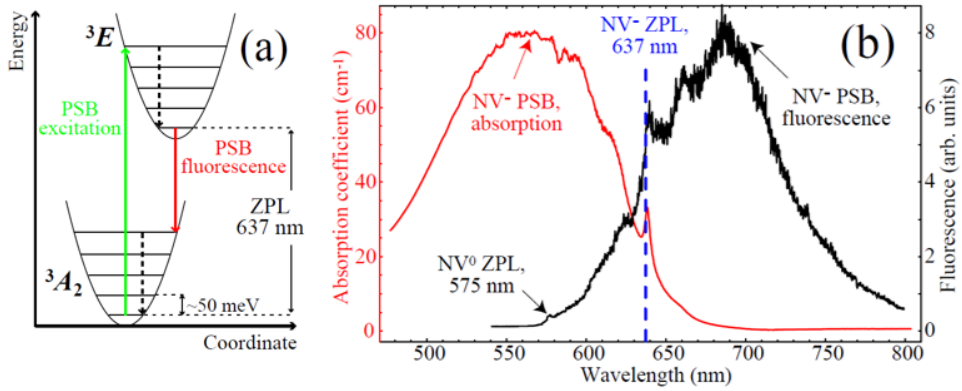

Figure 1.3: Absorption and Fluorescence Spectra of the NV center. **(a)** The triplet ground and excited states of the NV center each have vibrations substates, which can be described as a simple harmonic oscillator where excitations corresponds to quanta of vibrational energy (phonons). The transition between the ground and excited states that produces or consumes no phonons corresponds to a photon with wavelength 647 nm, known as the zero phonon line (ZPL). A green photon can excite an NV center from the ground state to the excited state by creating phonons, which rapidly decay, leaving the NV in the lowest energy vibrational substate of the excited state. From the excited state, the NV center can emit a red fluorescent photon by decaying into a vibrational excited state of the ground state, where it rapidly decays to the vibrational ground state. **(b)** The maximum coupling occurs in the phonon side band (PSB), corresponding to green light ($\approx$ 550 nm) for absorption and red light ($\approx$ 700 nm) for fluorescence. Reprint from [7], used with permission.

1.2.3 Intersystem Crossing and RF Transitions

Another result of the phonic sidebands is the coupling of the singlet and triplet states through a phenomenon known as Intersystem Crossing (ISC). ISC refers to the non-radiative process by which the spin multiplicity is changed (ie. $S = 1 \rightarrow S = 0$). In the case of NV centers, an NV in the excited (triplet) state (^3E) may, instead of emitting a photon, decay non-radiatively into the excited singlet state ($^1A_1$), made possible by the phonic sideband. From there, the NV will rapidly decay to the metastable singlet state (^1E), sometimes emitting an infrared photon in the process, where it will eventually decay to the (triplet) ground state ($^3A_2$) through ISC once again.

The remarkable thing about this process, is that the rate or probability at which the ISC occurs depends on the spin projection state: an NV in the excited state with $m_s = \pm 1$ is significantly more likely to decay to the singlet states than an NV with $m_s = 0$ [8]. Conversely, the metastable singlet state has a roughly equal probability into decaying into any of the three ground state sublevels. This has two very important consequences.

1. An NV center in the excited state with an equal probability in being in each of the three spin sublevels will have an increased probability of being in the $m_s = 0$ state after returning to the ground state. Through cycling the NV center between the ground and excited states many times, we can achieve spin polarization of the NV center through purely optical means, a technique known as optical pumping.

2. An NV center in the excited triplet state will on average give off more photons when it is in the $m_s = 0$ spin sublevel, compared to when it is in one of the other two spin states ($m_s = \pm 1$). This is the underlying principle for optical readout of the spin state.

The final piece of the puzzle is the manipulation of the spin state. After polarizing the spin via optical pumping, a coherent superposition of $m_s = 0$ and $m_s = +1$ (or -1) can be obtained by tuning microwaves to the resonant frequency of the $m_s = 0(or\text{-}1) \rightarrow +1$ transition. For a magnetic field aligned to the NV axis, that frequency can be described by the following expression.

$$\begin{aligned} f_{res} &= D \pm g_e \mu_B B_z \\ &= 2.87\,\text{GHz} \pm \left(2.8\,\frac{\text{MHz}}{\text{G}}\right) B_z. \end{aligned} \tag{1.3}$$

For magnetic fields not aligned to the NV axis, the energy eigenstates will be mixtures of the $m_s = 0, \pm 1$ sublevels, and the energy eigenvalues and corresponding transition frequencies can be found by diagonalizing the Hamiltonian.

1.2.4 Optically Detected Magnetic Resonance

Utilizing these phenomena, a simple experiment can be performed to detect the magnetically-sensitive microwave transition. This is achieved by sweeping the microwave frequency

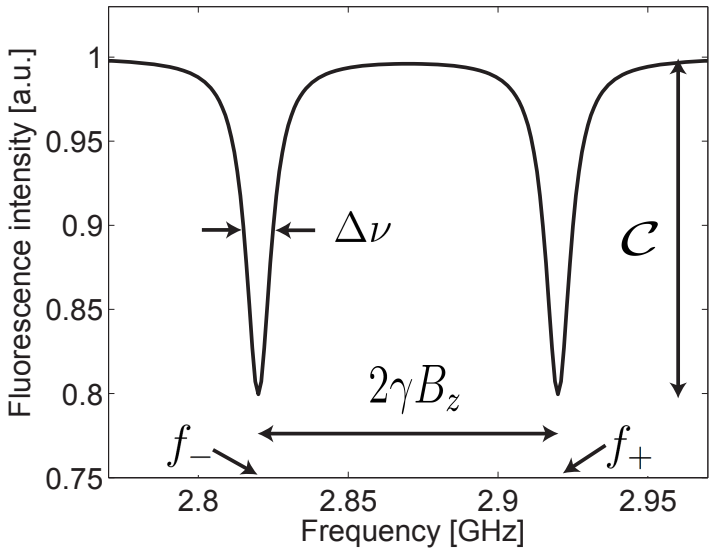

Figure 1.4: Optically detected magnetic resonance (ODMR) for a single NV center in the presence of a magnetic field aligned to the NV axis. The two resonant frequencies correspond to $m_s = 0 \rightarrow -1$ and $m_s = 0 \rightarrow +1$ transitions. Reprint from [9], used with permission.

through the resonant $m_s = 0 \rightarrow +1$ transition, while simultaneously pumping with green light and detecting the red fluorescence. The result is a decrease in the fluorescence of the NV center when the microwaves are resonant, or optically detected magnetic resonance (ODMR) [9]. For a single NV center, the linewidth is determined by the coherence time, T_2. For an ensemble of NV centers, the observed coherence time is denoted as T_2^*, and is typically much larger than that of a single NV center, due to inhomogeneities of the magnetic field. Since the resonant microwave frequency depends on the magnetic field (Eqn. 1.3), the resonant frequency can be fitted to determine the strength of the magnetic field along the NV axis. By introducing a large bias field, typically of strength ranging from 20 G to 50 G, we can ensure that the magnetic field stays aligned to the NV axis (a requirement for m_s to be a good quantum number), and measure changes in B_z. Magnetometery performed using this technique is known as continuous-wave (CW) magnetometry.

Another method for measuring the magnetic field involves microwave pulses. Instead of having two competing processes occurring simultaneously—optical pumping to $m_s = 0$ and microwave mixing from $m_s = 0$ back to $m_s = 1$—they are performed one at a time. First, the system is optically pumped into the $m_s = 0$ state. Then the laser is switched off, and a short pulse of resonant microwaves is applied creating an equal superposition of $m_s = 0$ and $m_s = 1$. This microwave pulse is known as a $\pi/2$-pulse, because it rotates the spin polarization on the Bloch sphere by an angle of $\pi/2$ [10]. This superposition, corresponding to a spin in the x-y plane, will precess at a frequency corresponding to the energy difference of the states. By applying a second microwave pulse at a later time, and then reading out

the spin state, a measurement of the precession frequency, and thus the magnetic field, may be obtained.

In terms of sensitivity, this pulsed magnetometery method performs similarly to cw magnetometery, except when tasked with measuring alternating current (AC) magnetic fields, where it is significantly superior. A simple method for measuring AC magnetic fields involves the use of a Ramsey pulse sequence, which can be described as follows. The superposition state is prepared using optical pumping and the application of a $\pi/2$-pulse, as discussed previously. It is then allowed to evolve for some time τ, after which, a π-pulse is applied, inverting the spins as well as any precession from the magnetic field. After waiting an additional time interval of length τ, another $\pi/2$-pulse is applied, and the projection of the spin is read out. This technique is maximally sensitive to AC magnetic fields of frequency $f = 1/(2\tau)$, with the added benefit of canceling out all constant magnetic fields, including the inhomogeneous magnetic field experience by an ensemble of NV centers. As such, the sensitivity for an AC magnetometer is limited by T_2, rather than T_2^*, [11].

More contemporary methods for measuring AC magnetic fields employ more sophisticated pulse sequences in order to better decouple the sensing spins from the noisy environment, a technique known as dynamic decoupling [12].

1.3 Outline of Remaining Chapters

One of the main advantages of NV-based magnetometry when compared to competing methods is the large range of spatial resolution and scalability. One can use a single NV center to measure the magnetic field produced by the nucleus of nearby carbon-13 atoms within the diamond lattice [13], or one can use 10^{11} NV centers to detect very small (100 fT) but uniform magnetic fields [14]. By using an array of diamond-based magnetometers, one can measure spatial variations in the magnetic field and obtain magnetic images.

In the following chapters, I will discuss how NV-based magnetometry is used and adapted to create a diamond-based imaging magnetometer (Chapter 2), as well as a specific application of magnetic imaging (Chapter 3). In Chapter 4, I will discuss my contribution to a separate project that was originally inspired by diamond-based magnetometry, and in the final chapter, I will conclude and summarize my dissertation.

Chapter 2

Diamond-based Imaging Magnetometer

2.1 Motivation

NV-based magnetometery can be extended to produce magnetic images and characterize spatial variations in the local magnetic field. This is especially desirable when characterizing the magnetic field produced by a source positioned a distance from the NV centers comparable to the size of the image. Each pixel on the camera will map to a different section of the diamond, essentially forming a planar array of magnetometers. At each pixel, the detected fluorescence can be used in order to determine the local magnetic field, and when combined will form a magnetic image.

2.2 Diamond Preparation

The diamonds used were primarily electronic-grade, chemical vapor deposition (CVD) diamonds with a very low (part per billion) level of impurities. Diamonds were cut and polished into thin plates with typical dimensions of $3 \times 3 \times 0.1\,\mathrm{mm}$. Electronic-grade CVD diamonds have very low concentrations of nitrogen and naturally occurring NV centers. This is important because we only want fluorescence to occur from a thin plane of NV centers at the surface of the diamond. Fluorescence from the rest of the diamond would still reach the camera, but it would be out of focus, and would be a background signal, washing out the magnetic image.

In order to create a thin layer of NV centers at the surface, the diamonds are irradiated with high energy nitrogen ions, a processes referred to as implantation. The energy of the ions can be changed to control the depth of the layer of implanted nitrogen, and to produce a thin layer of nitrogen at the surface of the diamond. As a rule of thumb, the depth of the layer is $\approx 1\,\mathrm{nm/keV}$. By implanting with multiple energies, one can fabricate a layer of nitrogen with uniform density at the surface of the diamond.

Table 2.1: Implantation Parameters. Each diamond plate is irradiated with ^{15}N ions of various energies. The energies and corresponding doses are specified in the table.

Energy (keV)	Dose (cm^{-2})
10	$4 \cdot 10^{12}$
20	$6 \cdot 10^{12}$
35	$9 \cdot 10^{12}$
60	$1.4 \cdot 10^{13}$
100	$2.2 \cdot 10^{13}$

After implantation, the diamond will contain both substitutional nitrogen defects and vacancies. To form NV centers, the diamond is annealed, typically at temperatures between 600 and 1000 °C [15], which allows the vacancies to hop between lattice sites until they bind to a substitutional Nitrogen, forming an NV center.

2.2.1 SRIM Calculations

The Stopping and Range of Ions in Matter[1] (SRIM) is a collection of software packages used to simulate the interaction of ions with matter using Monte Carlo methods. Using the software, along with the the physical properties of diamond, we can generate a distribution of outcomes from an Nitrogen ion of a specific energy striking the surface of a diamond plate. Of particular interest to us are the 'Ion Ranges' and 'Damage Events' outputs. The ion ranges describes the expected distribution of the final depth of an incident ion, and damage events describes the distribution of vacancies created per incident ion.

SRIM calculations were performed for energies of 10 keV, 20 keV, 35 keV, 60 keV, and 100 keV. The ratio of the doses required to produce a uniform layer of nitrogen was determined for different combinations of the energies, and was found to be $1 : 1.5 : 2.3 : 3.5 : 5.6$ when using all 5 energies. The corresponding ion ranges and damage event plots are shown in Fig 2.1. Listed in Table 2.1 are the implantation parameters that were chosen using these results in order to produce a high-density ($7 \times 10^{18}\,cm^{-2}$) uniform layer of nitrogen, with a thickness of 100 nm at the surface of the diamond plate. The depth was chosen to be as large as possible, to maximize NV yield, but still remain small compared to both the wavelength of fluorescence light and the size of the magnetic field sources to be measured. ^{15}N was chosen, rather than ^{14}N, on account of its smaller nuclear spin multiplicity ($I_{15} = 1/2$, $I_{14} = 1$) [16]. The diamond could then be annealed to convert the nitrogen atoms into NV centers, forming a high-density planar array of NV centers that is suitable for imaging applications.

[1]The Stopping and Range of Ions in Matter. `http://www.srim.org/`

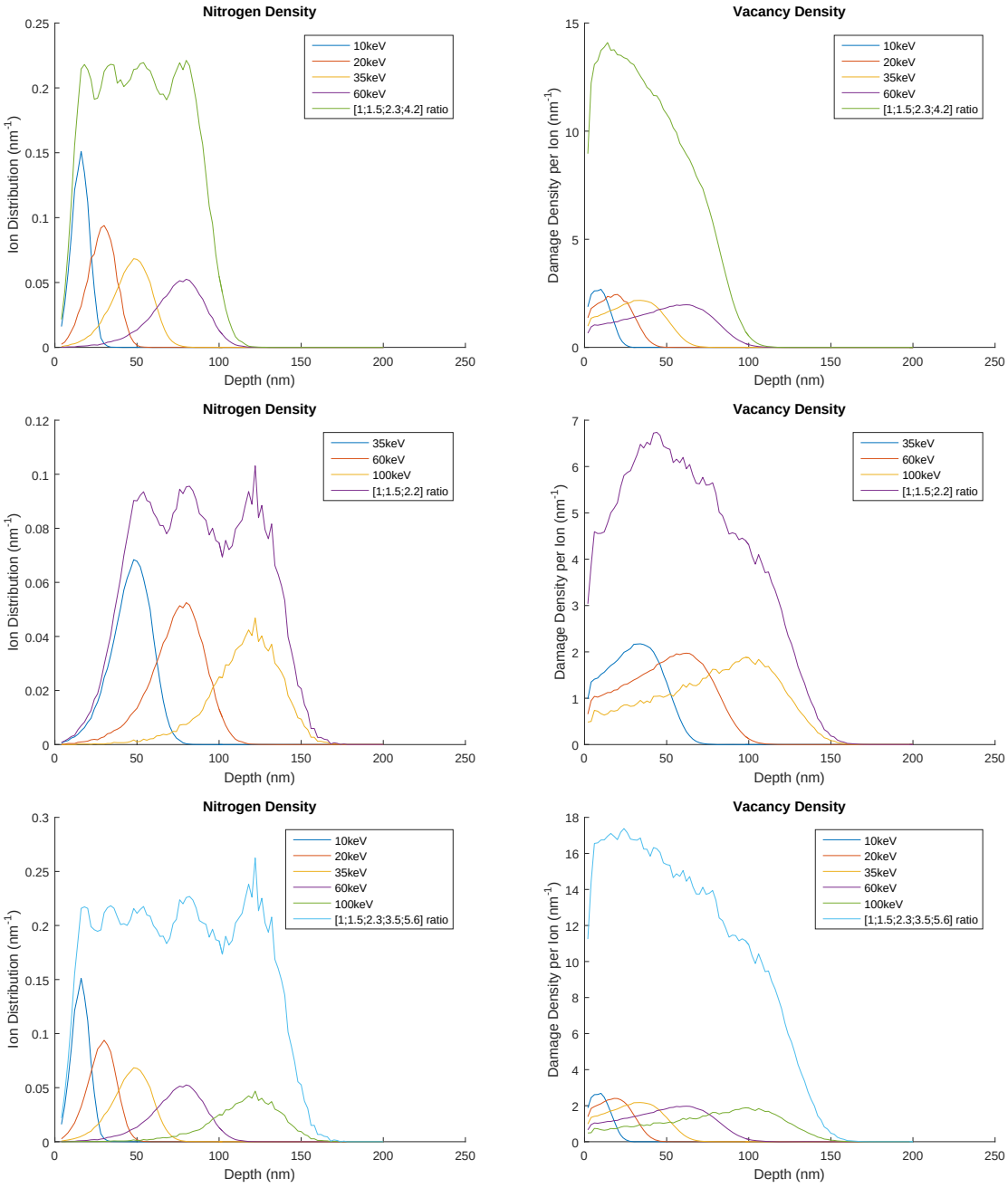

Figure 2.1: SRIM Calculations. Ion Ranges (left) and Damage Events (right) are plotted for various energies, and for a linear combination of all of the plotted energies with weights chosen to produce a uniform distribution of nitrogen.

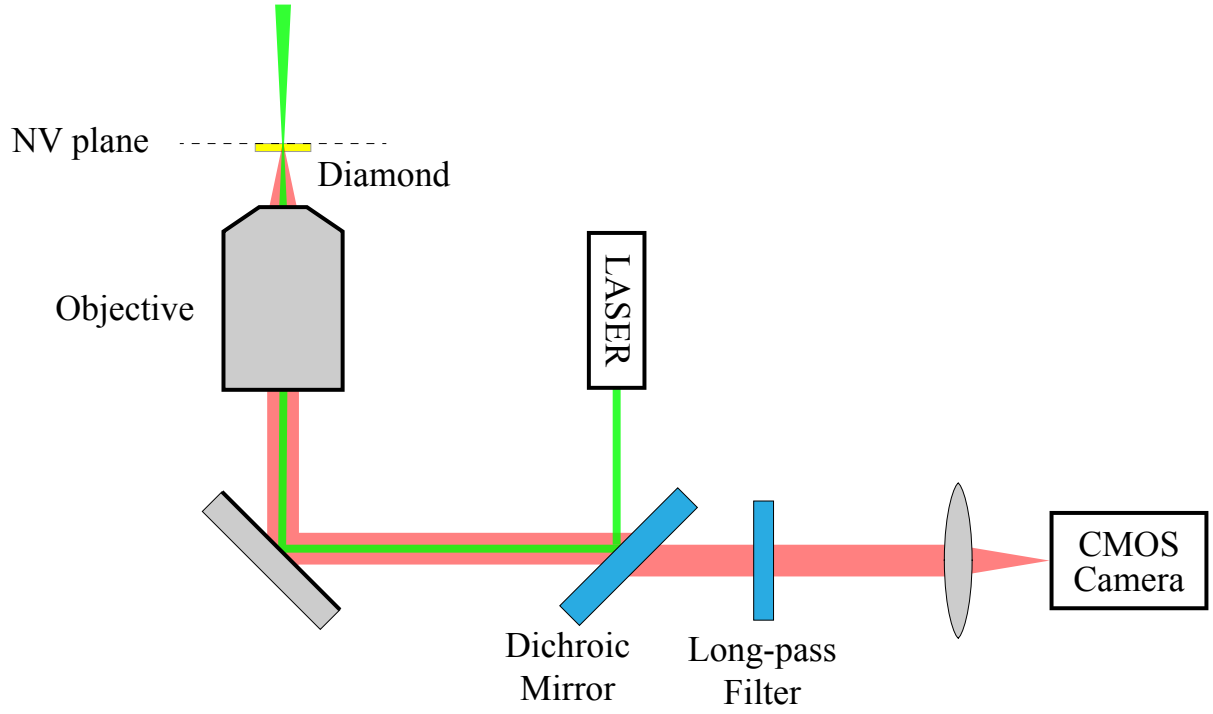

Figure 2.2: Optical Schematic for the diamond-based imaging magnetometer. The objective both provides the green the excitation from the laser and images the fluorescence from the NV plane onto the CMOS camera sensor. A dichroic mirror separates the beam path for the two wavelengths, and long-pass filter prevents any green light from reaching the camera. A defocusing lens (not shown) is positioned between the laser and the dichroic mirror in order to increase the size of the illuminated region on the diamond. Adapted from [17], used with permission.

2.3 Experimental Setup

2.3.1 Optics

A simplified schematic of the optical setup is shown in Fig 2.2.

The experimental setup for diamond-based magnetic imaging uses a shared microscope objective for both optical excitation and detection of fluorescence. The objective used for these experiments is a Nikon 40x objective (UPlanFL), which is an infinity corrected objective with working distance of 0.18 µm and a numerical aperture of 0.75. While objectives with higher numerical aperture, including oil-immersion objectives, are commercially available, and would provide significantly better magnetic sensitivity, the higher working distance was found to be extremely advantageous when working with certain samples.

The camera used was a complementary metal-oxide semiconductor (CMOS) Thorlabs camera (DCC1240M). While charge-coupled device (CCD) cameras are typically prefered in physics laboratories due to their lower read noise and better overall performance in dark environments, CMOS cameras are generally faster and perform well in bright environments. When combined with a tube lens with $f = 10\,\text{cm}$, the magnification of the objective/lens system was found to be 32, which after taking the camera pixel size into account (pixel size = $5.30\,\mu\text{m} \times 5.30\,\mu\text{m}$), corresponds to a conversion factor of $1\,\mu\text{m} = 6.0\,\text{pixels}$.

The laser used to provide the green excitation was a originally a 532 nm diode pumped solid state (DPSS) laser with maximum power of 200 mW. This laser was later exchanged for a 1 W 525 nm diode laser (Roithner Lasertechnik NLD5210000G). A defocusing lens is placed along the beam path before the dichoic mirror, in order to increase the size of the illuminated region on the diamond, effectively increasing the field-of-view at the expense of intensity and magnetic sensitivity.

A 550 nm dichroic mirror (Thorlabs DMLP550) is used to divide the optical path between the green excitation and the red fluorescence. To increase the optical separation between the two wavelengths, a 600 nm long-pass filter (Thorlabs FEL0600) is used to remove the laser light that manages to pass through the dichroic mirror. This is required because the large discrepancy in power between the excitation beam and fluorescence allows for a tiny fraction of the green light reaching the camera to drown out the fluorescence signal.

2.3.2 Microwaves

The power requirements for coupling microwaves to the system is quite low, and as a result, a simple solution is sufficient for our needs. For our experiments, a thin loop of copper wire (diameter 0.25 mm) is connected to the end of an SMA coax cable, shorting the cable. The loop is positioned using a 3D translation stage to bring to the surface of the diamond near the illuminated spot, using near-field coupling. Since the coupling depends on the distance between the NV centers and the loop, decreasing the distance can help lessen the power requirements for the microwaves. It is also important that the loop be short, compared to a wavelength. A long loop will be seen as a change in impedance of the cable, and the microwaves will reflect off of the interface before reaching the NV center.

For microwave generation, the main requirement is a frequency range of roughly 2.4 GHz to 3.2 GHz. Programmable frequency sweeps are extremely useful as well. The microwave generator primarily used for experiments is SynthNV from Windfreak. The generated microwaves are amplified by an RF amplifier (Minicircuits ZVE-3W-83+ or ZHL-15W-422+), sent through a circulator to protect the amplifier from the reflected power, and then delivered to the NV centers.

2.3.3 Magnetic Field

To produce the required magnetic field, a permanent magnet with surface field strength of 1 kG is used. Although a magnetic field produced from coils allows for more complex exper-

iments to be performed, applying large fields requires a significant amount of engineering, when a permanent magnet is often sufficient. Typical experiments with NV centers requires fields exceeding 10 G in order to sufficiently split the zero-field ODMR. For our experiments, the external magnetic field strength was typically chosen to be between 20 G and 100 G.

The magnetic field is aligned to one of the four NV axes, preferably the one that has the best coupling to the microwave field.

2.3.4 Imaging and Lock-in Detection

It is often very desirable to avoid measuring DC (direct current, ie. constant) signals, and instead obtain differential measurements. There are many places in the imaging magnetometer setup where environmental factors can cause the signal to drift. Some common sources of drift include temperature fluctuations and thermal expansion, air currents, ambient light levels, and electrical $1/f$ noise also known as flicker noise (not technically drift, but similar and still problematic).

To combat drift, we set up the camera to only image a signal every other frame. During the odd frames, the microwave signal is switched on, and during the even frames, the microwave signal is switched off. This technique, known as lock-in detection, is achieved by passing the microwaves through an RF gate that toggles between open and closed for alternating images via synchronized triggers. Rather than directly measuring the brightness of each pixel, we instead can obtain a contrast, by subtracting odd images from even images and then dividing by the even images. With this method, the microwaves can be swept through the resonant frequency as slow as we like, as the contrast images are insensitive to low-frequency drifts.

As an added benefit, this technique helps also reduce fixed-pattern noise in our CMOS camera. Each pixel of the camera can be thought of as its own photoreceptor with a fairly linear response curve. Let us assume that each pixel has a perfectly linear response, but is allowed to have a different responsivity, or ratio between output power and input power. If we obtain a contrast signal for each pixel, which is the measure of the fractional change in brightness, the responsivity of each pixel cancels out, resulting in a contrast image with significantly reduced noise when compared to the raw images.

In order to prevent the pixels from saturating, the camera is set to its maximum frame rate for the given area of interest (AOI), typically around 200 fps. In the interest of hard-drive space, which fills up quite rapidly when taking video at high framerates, software was written to interface with the camera and process images in realtime. After the image memory buffer filled up, the odd images were summed together, and the even images were summed together, and the single pair of images was recorded to the hard drive along with the relevant metadata, reducing the required hard disk space by roughly a factor of 100.

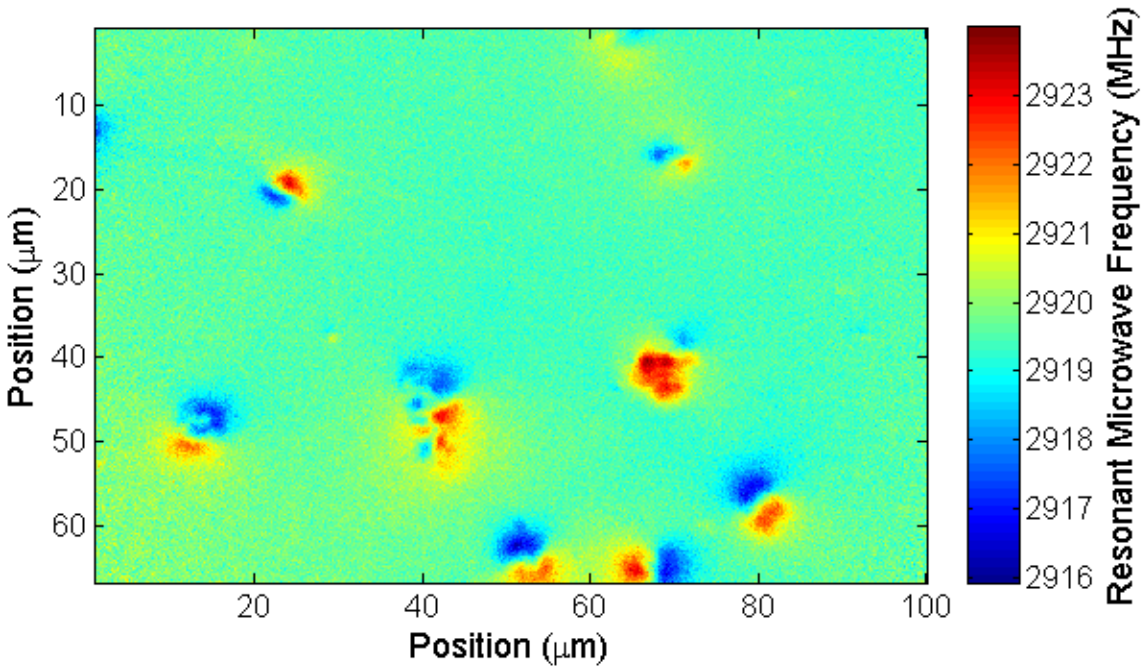

Figure 2.3: Magnetic image of ferromagnetic particles. A solution containing magnetized ferromagnetic particles of diameter 5 µm was allowed to dry on the surface of the diamond plate. The experiment was performed with a bias field of 18 G, using the methods described in this chapter.

2.4 Conclusion

After combining all of the previously described techniques, a contrast value is obtained at every pixel while sweeping the microwave frequency through the resonance. At each pixel, the ODMR is fitted to a double Lorentzian, split due to the spin of the ^{15}N nucleus, and the fitted resonant frequency for each pixel is combined into an image. An example of such an image is presented in Fig. 2.3, where several dry ferromagnetic microparticles of diameter 5 µm are visible on the surface of the diamond.

Chapter 3

An Application of Magnetic Imaging: Force-Induced Remnant Magnetization Spectroscopy

3.1 Introduction

Although normally one would search for solutions to existing problems, in experimental physics one often has solutions in need of problems to solve. After developing a technique that produces images of the local magnetic field with diffraction-limited resolution, the next step was finding a useful application. Among several alternatives, the application I settled on was Force-Induced Remnant Magnetization Spectroscopy.

Force-Induced Remnant Magnetization Spectroscopy (FIRMS) is a technique for quantitatively measuring the bonding force between specific receptor-ligand pairs [18, 19]. Suppose we are interested in studying the interaction between biomolecules A and B. Performing FIRMS with biomolecules A and B can be described as the following sequence of steps.

1. Microscopic magnetic beads are functionalized with biomolecule A, and a substrate is functionalized with biomolecule B.

2. The beads are allowed to bind with the substrate in solution, where they are magnetized using a strong magnet.

3. A force is applied to the system, typically using a centrifuge, mechanical shaker, or ultrasonic transducer, which causes some of the bonds to rupture, detaching the beads to detach from the substrate. Once a bead has been detached, it will have a random orientation, even if it rebinds to the surface.

4. The remnant magnetic field produced by the magnetic beads is then measured using an atomic vapor-cell magnetometer, and the fraction of the beads that have been detached from the surface can be determined.

5. The force application and magnetic field measurement (steps 3-4) are repeated with progressively larger forces, resulting in a force spectrum, used to characterize the interaction between A and B.

FIRMS was pioneered by Shoujun Xu, a former post-doc of the Budker group. In this chapter, I will present an adaptation of this technique using imaging and NV centers, based on work reported on in [17].

3.1.1 Motivation

FIRMS has conventionally been performed using a vapor-cell magnetometer, which has a sensor size on the order of millimeters. As a result, the detected magnetic field is quite small, typically 3×10^{-14} T. Since the magnetic field produced by a dipole scales with $1/r^3$, large gains in signal strength can be achieved by using a magnetometer with higher spatial resolution and detecting the field much closer to the magnetic beads. Diamond-based magnetometry is a strong candidate for such a detection scheme, allowing for the resolution of individual magnetic beads.

To move the sensor as close as possible to the magnetic beads, we chose to use the diamond itself to be the substrate on which the magnetic beads would bind. As a first step, we chose to study the biotin-streptavidin interaction, on account of its well-characterized interaction [20, 21, 22].

3.2 Surface Preparation

In order to prepare the diamond surface to interact with streptavidin coated magnetic microbeads, the surface of the diamond needs to be functionalized with biotin molecules. Functionalization is the process in which the surface termination of the diamond is replaced with a functional group, forming a covalent bond to the carbon lattice [23]. In the case of biotin functionalization, the functional group possesses a biotin molecule.

Functionalizing a diamond surface is something that our lab is not equipped to do. We received help from Olga Shenderova and Marco Torelli at Adamas Nanotechnologies[1], who performed the biotin functionalization on our behalf. They performed functionalization with a polyethylene glycol (PEG) layer between the diamond surface and the biotin. We also have control diamonds functionalized, where the surface was prepared in an identical fashion, except without the final step of adding the biotin molecules.

3.3 Microfluidics

The original iterations of the experimental setup are depicted in Fig 3.1. The diamond plate is attached using an adhesive (crystal wax) to a thin aluminum mounting plate ($15 \times 15 \times$

[1] Admas Nanotechnologies. `https://www.adamasnano.com/`

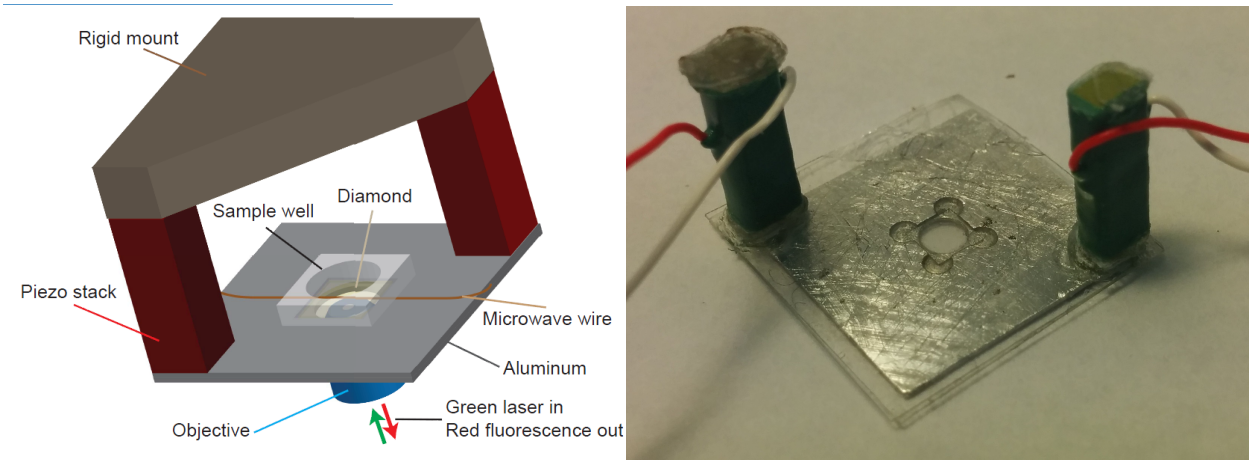

Figure 3.1: Schematic (left) and photograph (right) of early iterations of the chamber. The diamond plate is attached to a thin aluminum mounting plate with crystal wax. The aluminum mount has a circular hole for optical access from below, for both excitation with green light and detecting red fluorescence. The earliest iterations of the chamber used a sample well (left) to hold the solution. The next iterations (right) formed a chamber between the aluminum mounting plate and a glass coverslip using an imaging spacer. Piezo-electric actuators are mounted on opposite corners to apply the external force.

0.3 mm) with a 2 mm diameter hole for optical access. A square-shaped inset is drilled to bring the diamond closer to the lower surface of the aluminum, allowing for the use of an objective with a shorter working distance. For the adhesive, we used crystal wax, a non-fluorescence crystal with a low melting point. After mounting the diamond, a plastic sample well (3mm x 3mm x 1mm) is attached with adhesive (super glue) to the diamond. To deliver microwaves to the system, a thin wire is run a along the top surface of the diamond. The aluminum mounting plate is attached to a rigid mount by a pair of piezoelectric actuators, which are responsible for providing the force required to break the bonds between the microbeads and the diamond surface. Lastly, the saline solution containing the magnetic streptavidin-coated microbeads is added to the sample well, and the experiment is conducted.

The main difficulty with this method, and the reason it was ultimately replaced, was the evaporation of the fluid. A sizable fraction of the liquid was found to evaporate in tens of minutes, greatly limiting the extent of experimentation that could be performed. Furthermore, it was quite common for the seal between the diamond and mounting plate to be leaky, and have liquid build up on the lower surface of the diamond, which compromised the imaging.

For the second iteration of the setup, the goal was to create a sealed chamber, to prevent evaporation. The sample well was replaced with an imaging spacer (Invitrogen Secure

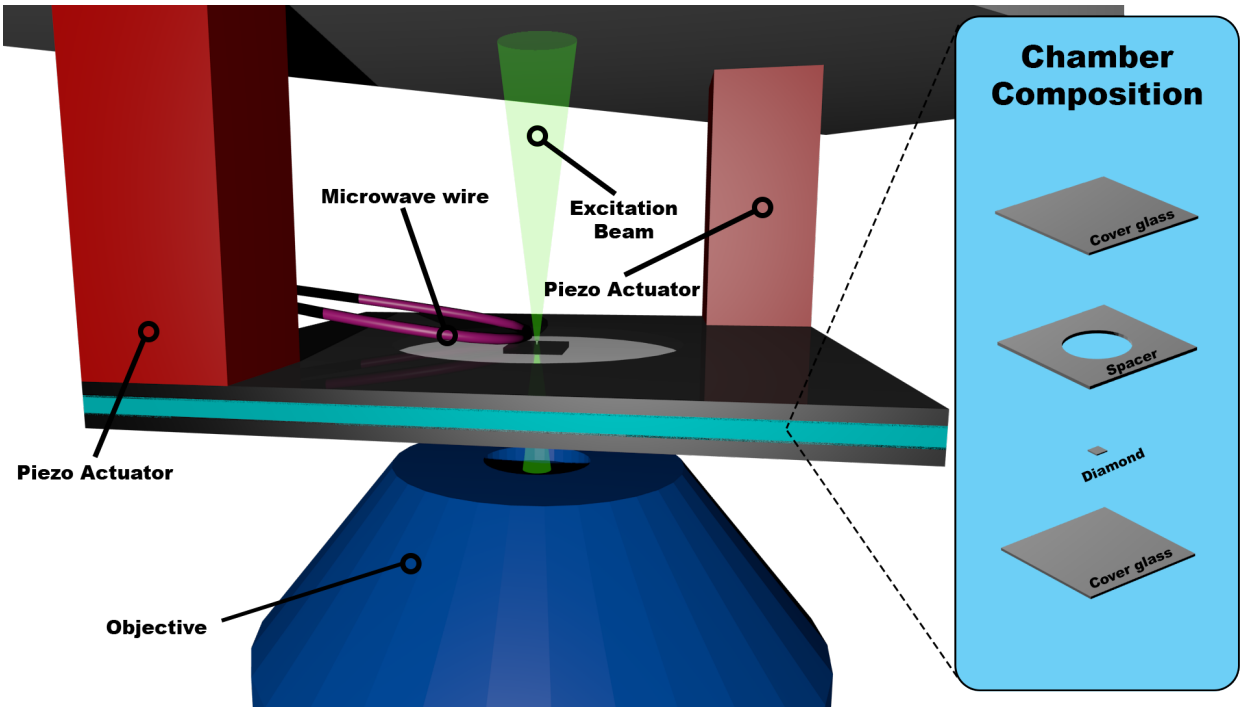

Figure 3.2: A 3D rendering of the final version of the chamber used in the experiments. The chamber is composed of and imaging spacer sandwiched between two glass coverslips with the diamond plate inside, attached to the lower coverslip using crystal wax. Microwaves are coupled to the system through a wire positioned on the top surface of the chamber. The chamber is connected to a pair of piezo-electric actuators, on opposite corners, which are connected to a rigid mount. Reprint from [17], used with permission.

Seal^{TM}), and a coverslip. These imaging spacers are essentially double-stick tape with a circlular hole cut out in the center. The photograph of the second iteration of the setup can be seen in Fig. 3.1. Although there were noticeable improvements over the first iteration, forming a good seal between the diamond and aluminum plate proved to be quite challenging, and the fluid often leaked through the lower surface of the diamond, which compromised the imaging.

In final version of the setup, the aluminum mounting plate was discarded in favor of sandwiching the diamond and imaging spacer between a pair of coverslips, forming a sealed cylindrical chamber. Before sealing the chamber, the diamond plate was attached to the lower coverslip using crystal wax, in order to prevent the diamond from moving around. The working distance of the objective (0.75 mm) was just large enough to focus on the upper (farther) surface of the diamond. A 3D rendering of the final iteration of the chamber is depicted in Fig. 3.2.

3.4 Force application using Piezo-electric Actuators

Three main factors that were considered when choosing a method of force application.

1. The strength of the maximum force that could be applied
2. The ability to apply a force in-situ
3. The degree of control (eg. drive frequency) over the force

While a centrifuge or mechanical mixer would allow for precise forces of large magnitude, the ability to obtain images of the magnetic particles while the force is being applied is very appealing. Although the maximum force that can be applied by piezo actuators is significantly smaller than the alternatives, this was outweighed by ability to apply a force over a wide range of frequencies, while also being able to apply a force without disturbing the imaging setup.

If we consider driving the piezo-electric actuator with a sinusoidal voltage, we would expect the surface of the diamond to move sinusoidally, $x(t) = x_0 \cos(\omega t) = x_0 \,\mathrm{Re}\{e^{i\omega t}\}$, with some maximum acceleration equal to $a_{max} = \omega^2 x_0$. For an ideal piezo-electric actuator with maximum displacement Δx, maximum voltage ΔV, and capacitance C, we can write down the displacement as a function of the voltage:

$$x_{piezo} = \frac{\Delta x}{\Delta V} V. \tag{3.1}$$

The chamber can be thought of as a mechanical oscillator with gain $G(\omega)$, which we can use to relate the voltage amplitude V_0 to the position of the diamond $x(t)$:

$$x(t) = \frac{\Delta x}{\Delta V} V_0 \cdot \mathrm{Re}\{G(\omega) e^{i\omega t}\}. \tag{3.2}$$

Note that generally, $G(\omega)$ is complex, and can introduce a phase between the voltage drive and the mechanical motion. In this case, we are only interested in amplitudes, so this detail can be ignored.

If our piezo drive is voltage limited, then the maximum acceleration immediately follows:

$$a_{max} = \frac{1}{2} \left(\frac{\Delta x}{\Delta V} \right) \omega^2 |G(\omega)| \cdot V_{max}. \tag{3.3}$$

The factor of two comes from the fact that V_{max} has a corresponding maximum amplitude of $V_{max}/2$.

If we assume that we are current limited, then we can calculate a corresponding maximum speed of diamond, making use of the fact that the amplitudes of charge Q_0 and current I_0

are related by a factor of ω,

$$v(t) = \frac{\Delta x}{\Delta V} V_0 \omega \,\mathrm{Re}\{G(\omega) i e^{i\omega t}\} \tag{3.4}$$

$$= \frac{\Delta x}{\Delta V} \left(\frac{I_0}{C}\right) \mathrm{Re}\{G(\omega) i e^{i\omega t}\} \tag{3.5}$$

$$v_{max} = \left(\frac{\Delta x}{C \Delta V}\right) |G(\omega)| I_{max}, \tag{3.6}$$

which can be related the maximum acceleration using $a_{max} = \omega v_{max}$:

$$a_{max} = \left(\frac{\Delta x}{C \Delta V}\right) \omega |G(\omega)| \cdot I_{max}. \tag{3.7}$$

If we wish to maximize acceleration when voltage limited, we should to use a piezo-electric actuator with the smallest voltage per length ratio, to maximize the distance per Volt. If we wish to maximize acceleration when current limited, we should use a piezo-electric actuator with the smallest charge per length ratio, to maximize the distance per unit of charge.

The piezo-actuators used in this experiment were primarily Thorlabs AE0203D08F. Before a 1 A piezo driver was obtained (Thorlabs BPC303), efforts were made to maximize the applied force using a more conventional 60 mA driver (Thorlabs MDT694B). Several different models of piezo-electric actuators were considered. Table 3.1 lists a summary or properties and derived quantities of these piezo-electric actuators, including calculations of the maximum acceleration assuming $G(\omega) = 1$.

3.4.1 Interferometer

The mechanical motion of the chamber is converted into in a force on a magnetic microbead through the microbead's own inertia, which pulls on the bonds when the chamber is at the apex of its motion. As such, the applied force should be proportional to the amplitude of the mechanical oscillation of the system, which in turn we expect to be linear in applied voltage. The amplitude of the oscillations of the mechanical system was measured using an interferometer, allowing the linear response to be verified, and the linear coefficient to be obtained. With the measured amplitude and the known drive frequency, a force per unit mass, or g-force, can be calculated. This allows us to map the applied force on a magnetic microbead as a function of frequency and voltage applied with the piezoelectric actuators.

In order to obtain the full picture of the mechanical motion of the system, some diagnostic must be performed to learn about the mechanical response of the system. To do so, the configuration of the optical setup was changed to that of a Michelson interferometer. The dichroic mirror was replaced with a beam splitter, an additional mirror and graduated neutral density filter were added to create the second arm of the interferometer, the long-pass filter was removed, and a flip mirror was used to swap detection from the camera to a photodiode

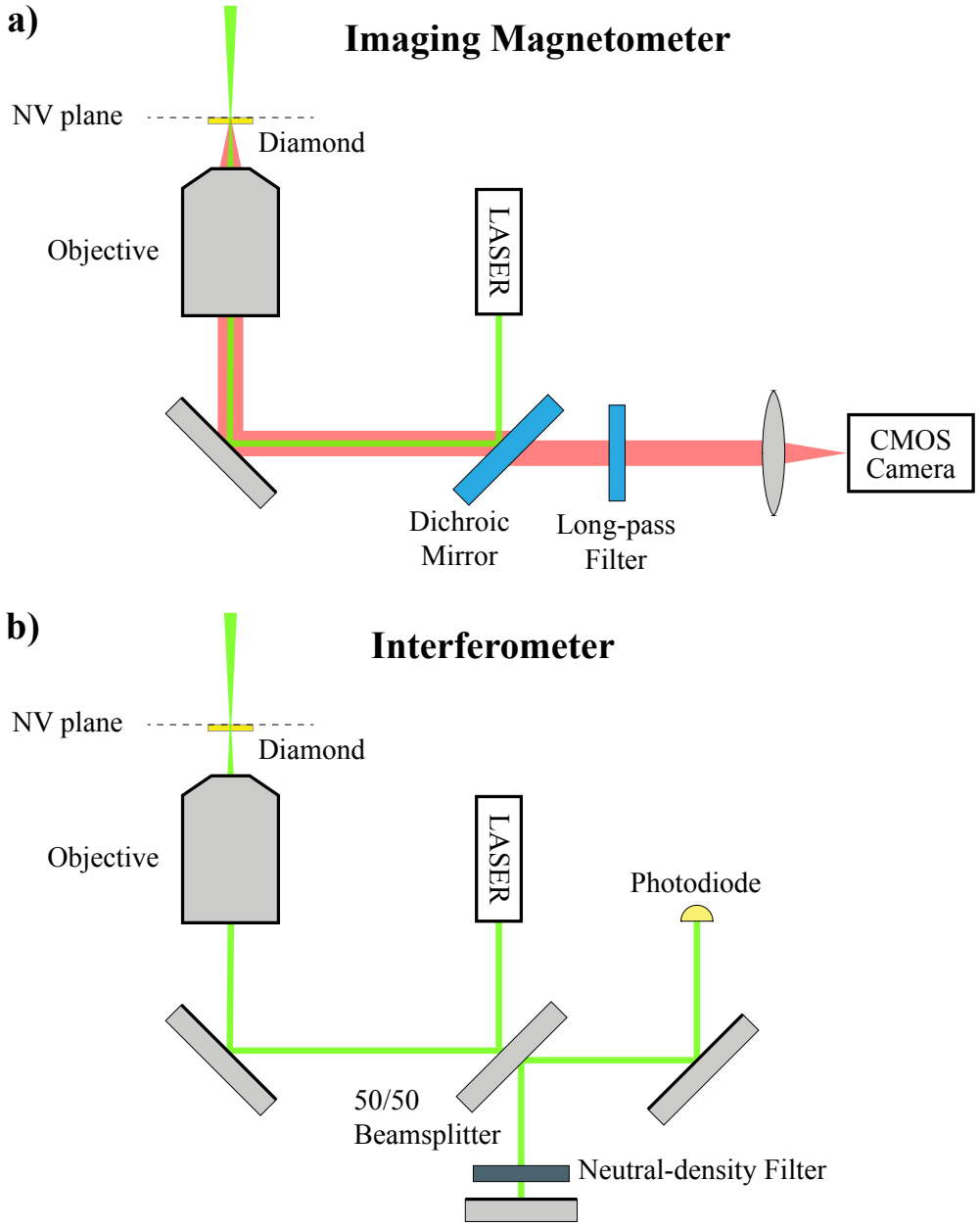

Figure 3.3: Optical schematic for the imaging magnetometer (top) and interferometer (bottom). To switch to the interferometer setup, the dichroic mirror is replaced with a beam splitter, and the second arm of the interferometer is formed with a mirror and graduated neutral density filter. The graduated neutral density filter was adjusted to match the reflect intensity of the two arms of the interferometer. Lastly, the long-pass filter is removed and a flip mirror redirects the beam to a photodiode. Reprint from [17], used with permission.

		Properties			Derived Quantities			
	Thorlabs	V_{max}	Δx	C	$\Delta x/V_{max}$	$\Delta x/Q_{max}$	a_{max} (g)	
#	Part Number	(V)	(µm)	(nF)	(µm/kV)	(µm/µC)	60 mA	1 A
1	AE0203D08F	100	6.1	180	61	0.34	260	2200
2	PA4CEW	150	2.0	22	13	0.61	400	810
3	PA2AD	75	1.1	15	15	0.98	440	440
4	PA2AB	75	0.7	9	9.3	1.04	280	280

Table 3.1: Properties and derived quantities for various piezo-electric actuators. The properties include the maximum voltage V_{max} corresponding to a voltage range of $[0, V_{max}]$, the range of the actuator Δx, and its capacitance C. The derived quantities include characteristic constants for displacement per volt (voltage-limited) and displacement per charge (current-limited). Also included is the maximum acceleration, measured in units of g ($9.8\,\mathrm{m/s^2}$), for piezo drivers possessing current limits of 60 mA and 1 A, with a drive frequency of 10 kHz. For these values, calculations are done assuming a mechanical gain of unity ($|G(\omega)| = 1$) and assuming an in-phase drive of a pair of piezo-electric actuators (same type), connected either in series or parallel, whichever produces the higher acceleration.

(Fig 3.3). The photodiode signal is amplified with a current amplifier (SRS570), while maintaining a bandwidth of 200 kHz, and subsequently recorded with an oscilloscope.

In an interferometer, the two interfering beams produce an electric field and intensity at the output that can be written as [24]

$$\begin{aligned} E(t) &= Re\{E_1 e^{i\omega_0 t} + E_2 e^{i(\omega_0 t+\phi)}\} \\ &= [E_1 + E_2\cos(\phi)]\cos(\omega_0 t) + [E_2\sin(\phi)]\sin(\omega_0 t), \end{aligned}$$

$$\begin{aligned} I(t) &= \langle E(t)^2\rangle \\ &= \frac{1}{2}[E_1^2 + E_2^2 + 2E_1E_2\cos(\phi)], \end{aligned} \tag{3.8}$$

where E_1 and E_2 are the two interfering fields, ω_0 is their angular frequency, and ϕ is the phase difference between the two arms of the interferometer. The angular frequency is related to the wavelength of the light, λ, by $\omega_0 = 2\pi \cdot c/\lambda$. Furthermore, the phase difference ϕ can be broken into two parts: the ideally constant piezo-independent phase distance ϕ_0, and a term governed by the mechanical response to the piezo-electric drive voltage, $V(t)$. If $V(t)$ is changed slowly enough such that the mechanical system can keep up ($G(\omega) \approx 1$), after removing the DC component, the predicted detected oscilloscope voltage signal, proportional

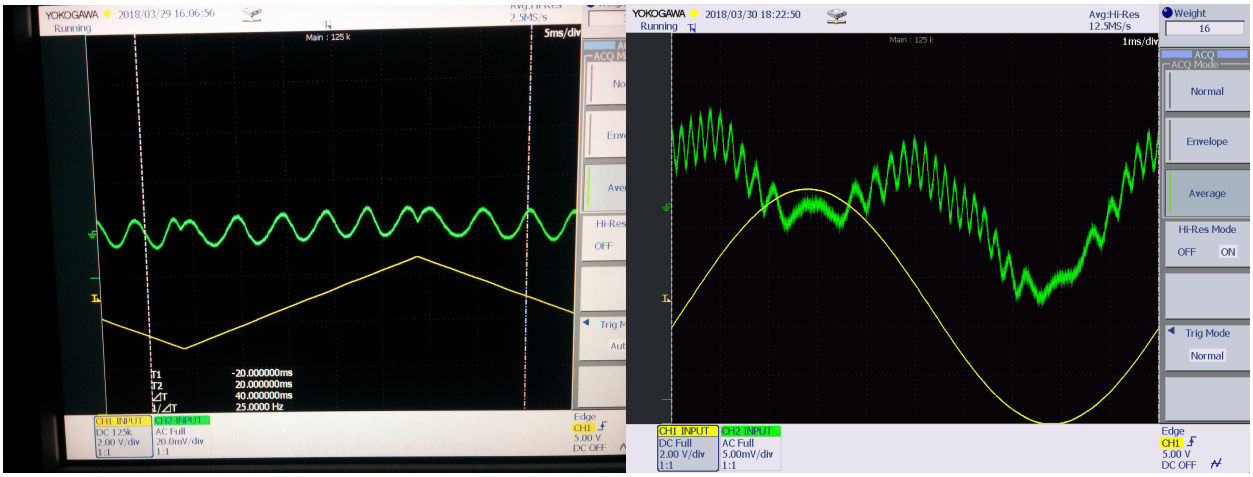

(a) Linear drive. (b) Sinusoidal drive.

Figure 3.4: Interferometer photodiode output during linear **(a)** and sinusoidal **(b)** drives at low frequencies. Under a linear drive ($f = 20\,\text{Hz}$), the photodiode signal is sinusoidal, and the distance travelled can be measured by counting the oscillations. Under sinusoidal drive ($f = 100\,\text{Hz}$), the photodiode signal oscillates rapidly when the drive signal is near the midpoint, and slowly when the drive signal is near the endpoints. At higher frequencies, the linear drive does not generally produce a sinusoid, due to a frequency dependent mechanical response. This can be seen in **(a)** at the endpoints, where the oscillations appear slightly slower immediately after reversing the drive direction.

to intensity, will be of the form

$$S(t) = S_0 \cos\phi(t) \tag{3.9}$$

$$= S_0 \cos\left(\phi_0 + \frac{2\pi}{\lambda}\frac{\Delta x}{V_{max}} V(t)\right), \tag{3.10}$$

where Δx and V_{max} are the range and maximum voltage of the piezo-electric actuator, respectively. If $V(t)$ is a triangle wave we would expect that the detected signal would be sinusoidal, with phase reflections when the triangle wave reaches its endpoint. In Fig. 3.4a, the piezo-electric actuators were driven together with a 20 Hz triangle wave, which is shown on the oscilloscope along with the detected photodiode signal.

If instead, the pizo-electric actuators are driven with a sinusoidal signal, the resulting output is a sine-of-a-sine

$$\phi = \phi_0 + \frac{2\pi x_0}{\lambda}\cos(2\pi f_0 t) \tag{3.11}$$

$$V(t) = V_0 \cos(\phi_0 + N\cos(2\pi f_0 t)), \tag{3.12}$$

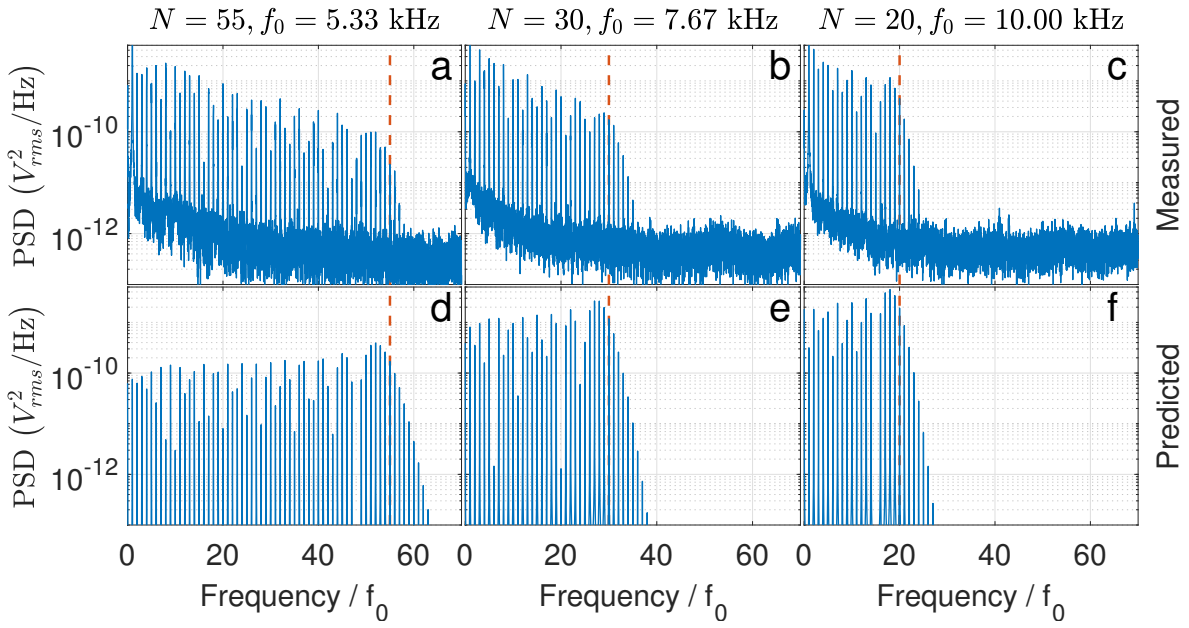

Figure 3.5: Power spectral density (PSD) of experimental photodiode data (a,b,c) alongside PSD of simulated data (d,e,f) with parameters chosen to yield matching spectra. The experimental data were collected using piezo drive of 60 volts peak-to-peak at frequencies of 5.33 kHz (a), 7.67 kHz (b), and 10.00 kHz (c). In each figure, the frequency axis has been scaled by $1/f_0$, such that the drive frequency and its harmonics appear at integers, allowing the value for N to be read directly from the plot (dashed vertical line). The fitted value for N can then be used to obtain a measurement of the amplitude of the mechanical motion. Reprint from [17], used with permission.

where x_0 and f_0 are the amplitude and frequency of the motion of the system. Here N, which we have defined to be $\frac{2\pi x_0}{\lambda}$, can be estimated by counting the number of harmonics of f_0 before roll-off in the power spectral density (PSD) of $V(t)$. A 100 Hz sinusoidal drive along with its corresponding photodiode output are shown in Fig. 3.4b. In Fig. 3.5, The PSD of sample interferometer data (a,b,c) obtained under sinusoidal drive is displayed alongside the PSD of Eq. (3.12) (d,e,f), with matching values for N and f_0.

3.5 Results

After developing all of the supporting techniques, the final step was to put everything together and obtain wide-field optical and magnetic data on the binding of the microbeads to the diamond surface under increasingly large mechanical oscillations. The piezo-electric drive voltage was ramped from 0 to 50 V_{p-p} in steps of 2 V_{p-p}, with a duration of 60 seconds for each voltage step. In order to avoid substantial heating from the piezo-electric drive, the

system was driven with a 0.5% duty cycle, or one 5 ms pulse each second, totalling 60 pulses per voltage step. This procedure was repeated for several chambers using diamond plates with either biotin surfaces, or control surfaces.

3.5.1 Wide-field optical imaging

While the force is being applied, the wide-field images were obtained continuously using the DCC1240M camera ($\approx$ 25 fps) using white light illumination. The non-bound microbeads can be observed to move around randomly, experiencing Brownian motion. During each pulse, the non-bound microbeads can be observed to experience a 'kick', all in the same direction. The direction was found to change depending on the drive frequency, and varied from chamber to chamber. Sample video can be seen here: Sample Video.

Software was developed to facilitate the process of determining the number of particles that remain bound to the surface of the diamond as a function of time. The software allowed the user to play the video file at different speeds, annotate the video file with the location of each bound particle, and the time at which each particle detached (Fig. 3.6). Other features included comparing images from different times of the video by plotting them on top of one other with different color channels. Once the user has completed annotating the video file, it automatically generates a plot of the number of bound particles as a function of time, or as a function of applied voltage.

When considering whether a particles is attached to the surface, some human judgement is required. Some particles often appeared to be 'dangling' from the surface, and were observed to move while confined to a small region. Generally, particles that were observed to move by more than one particle radius were considered to be detached. Once a particle has been detached, it is no longer tracked, and any subsequent reattaching and detaching is ignored. Similarly, only particles that started bound to the surface are counted. Great care was taken in an attempt to be consistent with identifying detachment events across all data sets.

The most noticeable difference between the biotin and control surfaces was that the particles would bind significantly more strongly to the control surface than to the biotin surface. This initially might come as a surprise, because one might expect the specific bonds between biotin and streptavidin to be stronger than non-specific binding between the particles and control surface. However, with both the number of bonds and the natures of the non-specific binding unknown, our results are well within the bounds of our expectations. Results from typical experimental runs are shown in Fig. 3.7.

Some variations were also observed between successive iterations of the experiment with different chambers, without switching between biotin and control surfaces. These variations were not as significant as the variations between biotin and control surfaces, and were also found to correlate with the mechanical response of the chamber measured using the interferometer (previously discussed). The mechanical response of the chambers used for Fig. 3.7 are shown in Fig. 3.8.

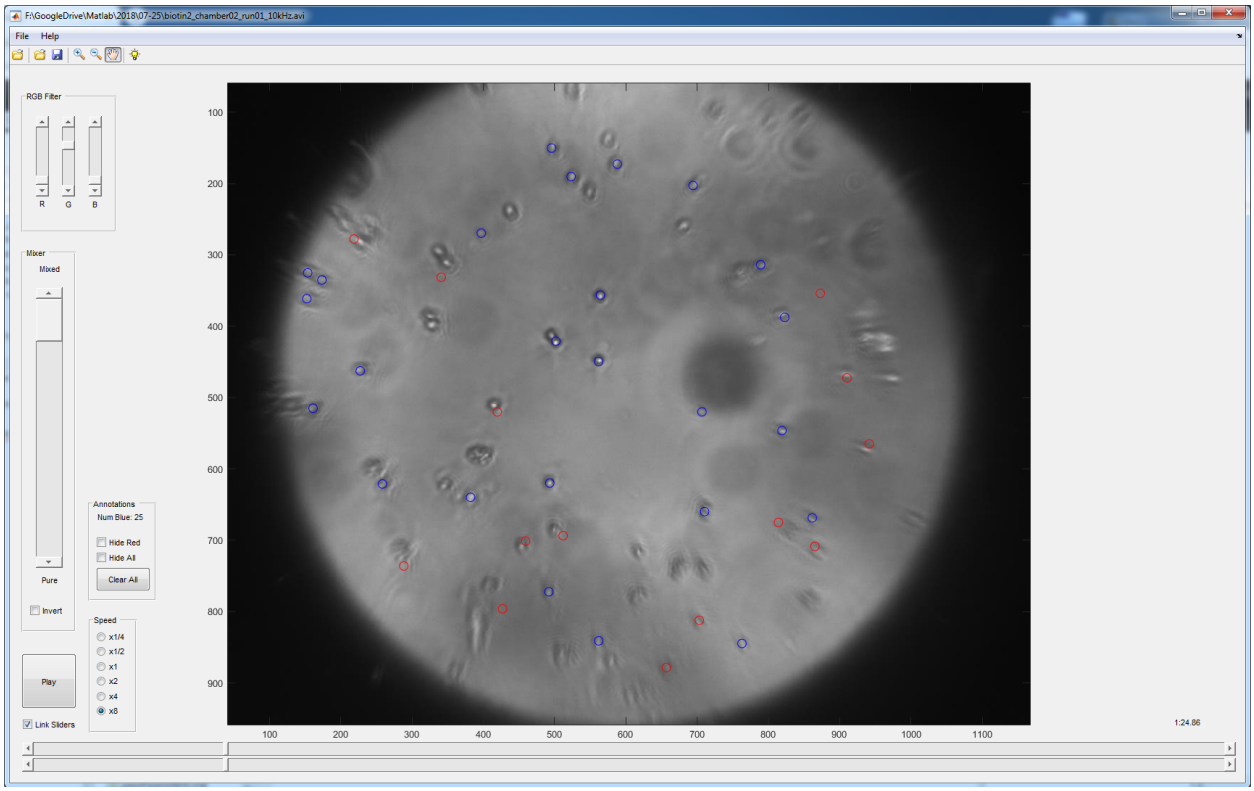

Figure 3.6: Particle tracking software. Software was created to facilitate identifying bound particles, and determining the time at which they detach from the surface. The software functions as a video player with multiple playback speeds, while also allowing to the user to display frame from two different times simultaneously using different color channels. Clicking on a location of the video creates a particle marker, and clicking again sets the current time to be the time at which the particle detached. This metadata can be saved and loaded as annotation files, which can also be used to automatically generate analysis plots.

In the literature, the bond strength between biotin and streptavidin is typically measured by linearly increasing the applied force at some rate, known as the loading rate, and measuring the rupture force, or force at which the bond is broken [20, 22, 25, 26]. This is somewhat different than what was done in this experiment, where the force applied is an oscillating force, whose amplitude is slowly ramped. If we calculate an 'effective loading rate' for our system, we can then compare our results to those in the literature. Using the method described in the following section, we estimate effective loading rate of our experiment to be 60 pN/ sec. Using results shown in Fig. 3.7 and Fig. 3.8, the rupture force for particles on the biotin surface was calculated to be 20(8) pN, which is a factor of 2-3 lower than that predicted by the literature values at similar loading rates [20, 21, 22, 25].

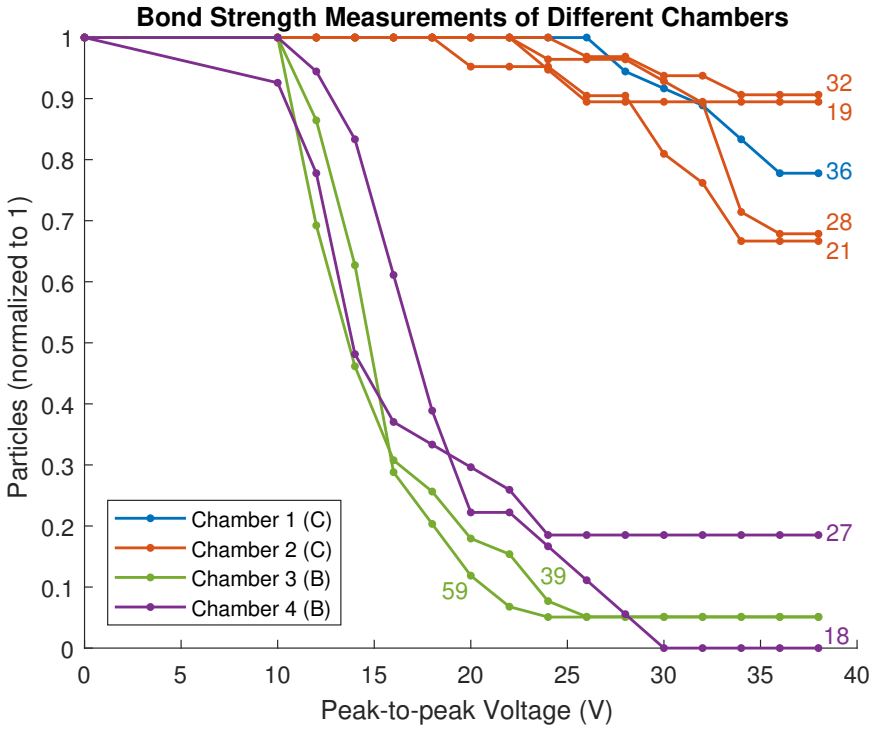

Figure 3.7: Normalized number of particles detached under increasingly larger voltages for various chambers. Particle positions were tracked under wide-field illumination as the voltage applied to the piezoelectric actuators was linearly ramped. The fraction of particles that remain bound to the surface is plotted against the drive voltage. The number of particles tracked during each experiment is indicated by a number labeling its corresponding line on the plot. Nine experiments were performed spanning four different chambers. Chambers with biotin surfaces are labelled with (B) and chambers with control surfaces are labelled with (C). Experimental runs for chambers 3 and 4 were performed at 5.5 kHz, while experimental runs for chambers 1 and 2 were performed at 10 kHz in order to maximize the force that could be applied in an effort to detach as many particles as possible. Reprint from [17], used with permission.

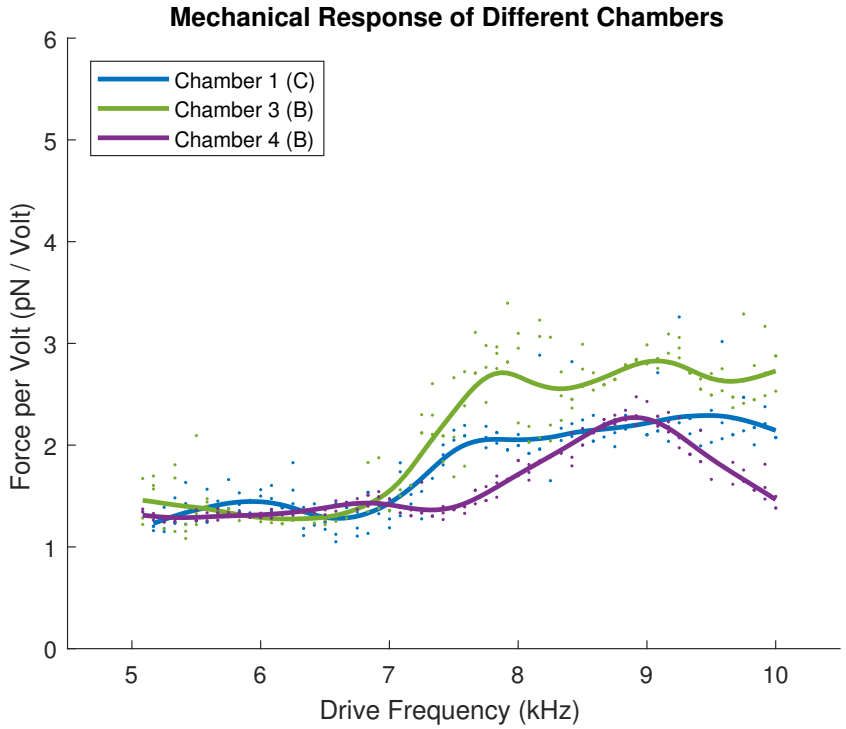

Figure 3.8: Amplitude of the force experienced by a microsphere with diameter 2 µm as a function of drive frequency for different chambers. The force amplitude (F) is calculated based on the sinusoidal amplitude of the mechanical motion (x_0), drive frequency ($\omega/2\pi$), and mass (m) according to the equation $F = m\omega^2 x_0$. Smoothing lines are added to highlight trends. Chambers with biotin surfaces are labelled with (B) and the chamber with a control surface is labelled with (C). Reprint from [17], used with permission.

3.5.2 Magnetic imaging

In a separate experimental sequence, magnetic imaging data were obtained. The excitation laser was positioned over three bound particles, and the magnetic field image was obtained before, during, and after applying the pulses (described previously) to the piezoelectric actuator (Fig. 3.9). The pulses were paused at 40 V_{p-p} in order to obtain the data for the "during" image, and the "after" image was obtained after ramping to 50 V_{p-p}. In the magnetic images, blue and red regions corresponding to positive and negative local magnetic fields with respect to applied external magnetic field, are clearly visible for each of the three particles, indicating the direction of the magnetic dipole of each particle. The maximum measured field strength is about $0.3\,\mathrm{G}$ ($3 \times 10^{-5}\,\mathrm{T}$), nine orders of magnitude larger than that typically detected when performing FIRMS using a vapor cell magnetometer ($3 \times 10^{-14}\,\mathrm{T}$).[18, 27] The magnetic images have highest uncertainty along the edges of the

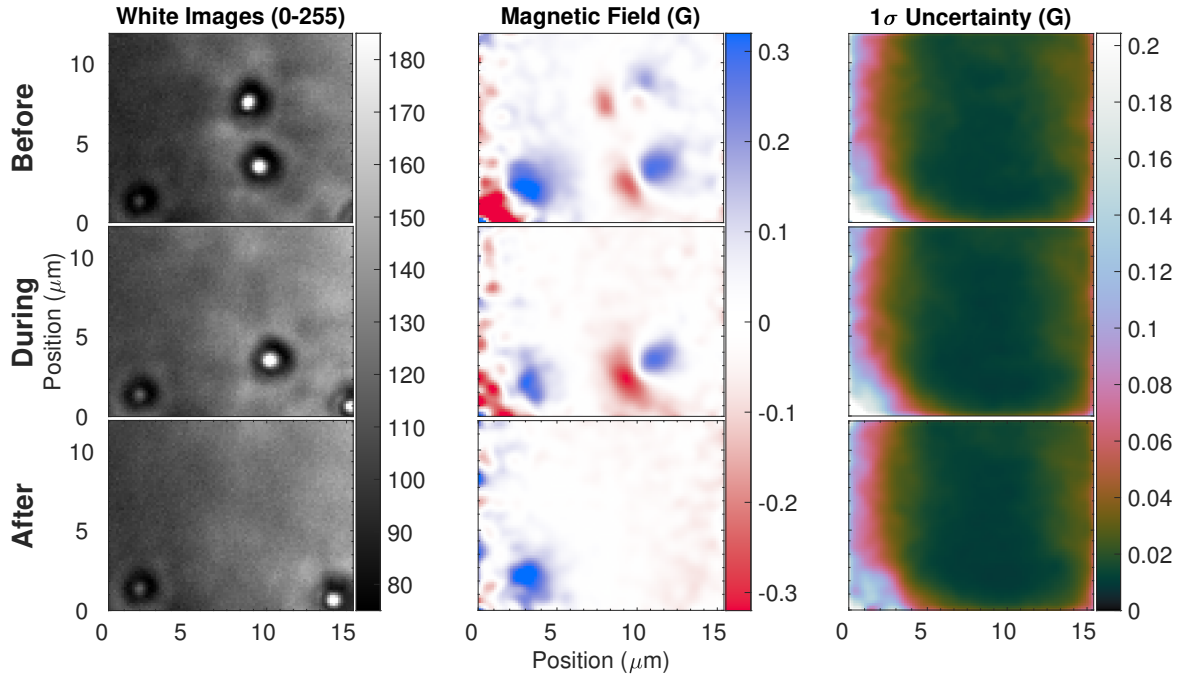

Figure 3.9: Images of particles before (top), during (middle), and after (bottom) application of force. Wide-field optical images are displayed on the left, where particles are visible as dark regions with Arago (Poisson) spots. Magnetic images are displayed in the middle with corresponding 1σ uncertainty displayed on the right. Magnetic images had an acquisition time of $\approx$ 10 minutes each, with a corresponding (unoptimized) sensitivity of $20\,\mu\mathrm{T}\sqrt{\mu\mathrm{m}^2/\mathrm{Hz}}$. Reprint from [17], used with permission.

images where the laser intensity was weakest. Magnetic microparticles that produce stronger magnetic fields are not used in order to reduce the particle-particle interactions.

3.6 Effective Loading Rate

We want to find the effective loading rate of an oscillating force that gradually grows in amplitude. We know that the loading rate for a non-oscillating force is rate at which the applied force increases. There should be some "conversion factor" between the rate at which the alternating force amplitude is increased and its effective loading rate, while maintaining the same rupture force.

3.6.1 Derivation of rupture rate

We assume a linear relationship, though only in a narrow range, between the rupture force and the log of the loading rate [26]. First we assume a reference point around which this assumption should hold: a loading rate of ν_R and a corresponding rupture force of F_R

$$F - F_R = F_0 \left(\ln \nu - \ln \nu_R\right), \tag{3.13}$$

where F_0 is the linear coefficient. F_0 can be understood to be the amount we must increase F in order to obtain a corresponding increase of $\ln \nu$ by 1, or increase ν by a factor of e:

$$(F_R + F_0) - F_R = F_0 \left(\ln \left(e\, \nu_R\right) - \ln \nu_R\right) \tag{3.14}$$

$$F_0 = F_0 \left(\ln e\right) \tag{3.15}$$

$$F_0 = F_0. \tag{3.16}$$

The next step is to consider the rupture rate in the presence of a constant force. When loading at a rate of ν_R, the time window Δt over which there is a significant probability to detach is approximately given by the difference between the times when the applied force is $F_R \pm F_0$, so $\Delta t \approx 2F_0/\nu_R$. If we turn this interaction time into a rupture rate (k) we find

$$k_R = 1/\Delta t = \xi\, \nu_R/F_0, \tag{3.17}$$

where k_R is the rupture rate at applied force F_R, and ξ is some constant "fudge factor" on the order of 1 from this approximation that is related to exponential integrals. When we increase the applied force by F_0 we expect the rupture rate to increase by a factor of e. This allows us to extrapolate the rupture rate as a function of the force F over a range of forces in the vicinity of F_R:

$$k = \xi\, \frac{\nu_R}{F_0} \exp\left(\frac{F - F_R}{F_0}\right). \tag{3.18}$$

3.6.2 Constant and Sinusoidal Force Comparison

First let us define an expression for the rupture rate when a constant force F_1 is applied,

$$k_0 \equiv \xi\, \frac{\nu_R}{F_0} \exp\left(\frac{F_1 - F_R}{F_0}\right)$$

$$k_0 = \xi\, \frac{\nu_R}{F_0} e^{x - x_0}, \tag{3.19}$$

where we have made the useful substitutions of x and x_0 defined as follows:

$$x \equiv \frac{F_1}{F_0}, x_0 \equiv \frac{F_R}{F_0}. \tag{3.20}$$

Now we want to compare k_0 to the average/effective rupture rate when the applied force is given by:

$$F(t) = F_1 \cos \omega t \tag{3.21}$$

$$k(t) = \xi \frac{\nu_R}{F_0} \exp\left(x \cos \omega t - x_0\right). \tag{3.22}$$

Next we take the time average of the rate over a single oscillation

$$\langle k(t) \rangle = \frac{\omega}{2\pi} \int_{-\pi}^{\pi} \xi \frac{\nu_R}{F_0} \exp\left(x \cos \omega t - x_0\right) dt, \tag{3.23}$$

and Taylor expand $\cos(\omega t)$ around its maximum:

$$\langle k(t) \rangle = \frac{\omega}{2\pi} \xi \frac{\nu_R}{F_0} \int_{-\pi}^{\pi} \exp\left(x \left(1 - \frac{\omega^2 t^2}{2}\right) - x_0\right) dt \tag{3.24}$$

$$\langle k(t) \rangle = \frac{\omega}{2\pi} \xi \frac{\nu_R}{F_0} e^{x - x_0} \int_{-\pi}^{\pi} \exp\left(-\frac{x\,\omega^2}{2} t^2\right) dt. \tag{3.25}$$

Recognizing that this is an integral of a Gaussian, we can neglect the tails of the integral and use the following identity to approximate the integral:

$$\int_{-\infty}^{\infty} e^{-ax^2} dx = \sqrt{\frac{\pi}{a}}. \tag{3.26}$$

As the sinusoid nears its peak, the probability to rupture, $k(t)$, is approximated by a Gaussian whose width gets narrower for larger oscillation amplitudes:

$$\langle k(t) \rangle = \frac{\omega}{2\pi} \xi \frac{\nu_R}{F_0} e^{x - x_0} \sqrt{\frac{2\pi}{x\,\omega^2}} \tag{3.27}$$

$$\langle k(t) \rangle = \xi \frac{\nu_R}{F_0} e^{x - x_0} \frac{1}{\sqrt{2\pi x}}. \tag{3.28}$$

Finally, after substituting the value we obtained for the rupture rate for a constant force:

$$\langle k(t) \rangle = k_0 \frac{1}{\sqrt{2\pi x}}$$

$$\langle k(t) \rangle = k_0 \frac{1}{\sqrt{2\pi F_1 / F_0}}. \tag{3.29}$$

From this we have calculated that the effective rupture rate, or probability of rupture per unit time, for a sinusoidal force of amplitude F_1 is $\sqrt{2\pi F_1/F_0}$ times smaller than for a constant force of F_1. This means that in order to observe the same rupture force, we would have to use a loading rate that is $\sqrt{2\pi F_1/F_0}$ times slower.

3.6.3 Calculation Results

Plugging in the values, we obtain the following:

$$\sqrt{2\pi F_1/F_0} = \sqrt{2\pi(20\,\mathrm{pN})/(5\,\mathrm{pN})}$$
$$\sqrt{2\pi F_1/F_0} = 5. \tag{3.30}$$

In our experiments, we apply 5 ms pulses, once per second for a minute, combining to a total of 300 ms per force increment. At steps of 4 pN, this would put our unadjusted loading rate at 4 pN / 300 ms, or around 13 pN/s. However, the effective time the force was applied was 300 ms / 5 = 60 ms, resulting in an effective loading rate of 60 pN/s, putting us one order of magnitude above typical optical tweezer loading rates.

3.7 Dielectrophoresis

Another method of force application we explored for conducting FIRMS is dielectrophoresis (DEP), or the movement of dielectric particles polarized in a non-uniform electric field [28]. Using DEP, uncharged polarizable particles can be manipulated with a non-uniform AC electric field. In contrast to the force applied using piezo-electric actuators, the force produced by DEP is a local force, only affecting a section of the surface of the diamond.

A first-order approximation of the dielectrophoretic force is given by [29, 30],

$$\vec{F}_{DEP} = 2\pi\epsilon_m r^3 K \nabla \left|\vec{E}_{rms}\right|^2, \tag{3.31}$$

where ϵ_m is the relative permittivity of the surrounding medium, r is the radius of the particle, E_{rms} is the root-mean-squared value of the electric field, and K is the real component of the Clausius-Mossotti (CM) factor that defines the polarizability of the particle with respect to the surrounding medium. For a spherical particle, the CM factor is given by [31]

$$\mathrm{CM}(\omega) = \frac{\epsilon_p^* - \epsilon_m^*}{\epsilon_p^* + 2\epsilon_m^*}, \tag{3.32}$$

where $\epsilon_p^* = \epsilon_p - i\sigma_p/\omega$ and $\epsilon_m^* = \epsilon_m - i\sigma_m/\omega$ are the complex permittivities of the particle and the surrounding medium, respectively, ϵ_p and ϵ_m are the permittivities, σ_p and σ_m are the conductivities, and ω is the frequency of the applied oscillating electric field. Put simply, the DEP force is proportional to the gradient of the square the electric field, and the direction of the force depends on the frequency of the electric field.

In our experiments, the electric field gradient is applied using interdigitated electrodes (IDEs). The IDEs were fabricated on the surface of glass coverslip, which forms the ceiling of the microfluidic chamber such that the fluid is in contact with the IDEs. An illustration and description of the setup is provided in Fig. 3.10. While no quantitative force measurements were taken using the DEP setup, we were successful in manipulating the particles between

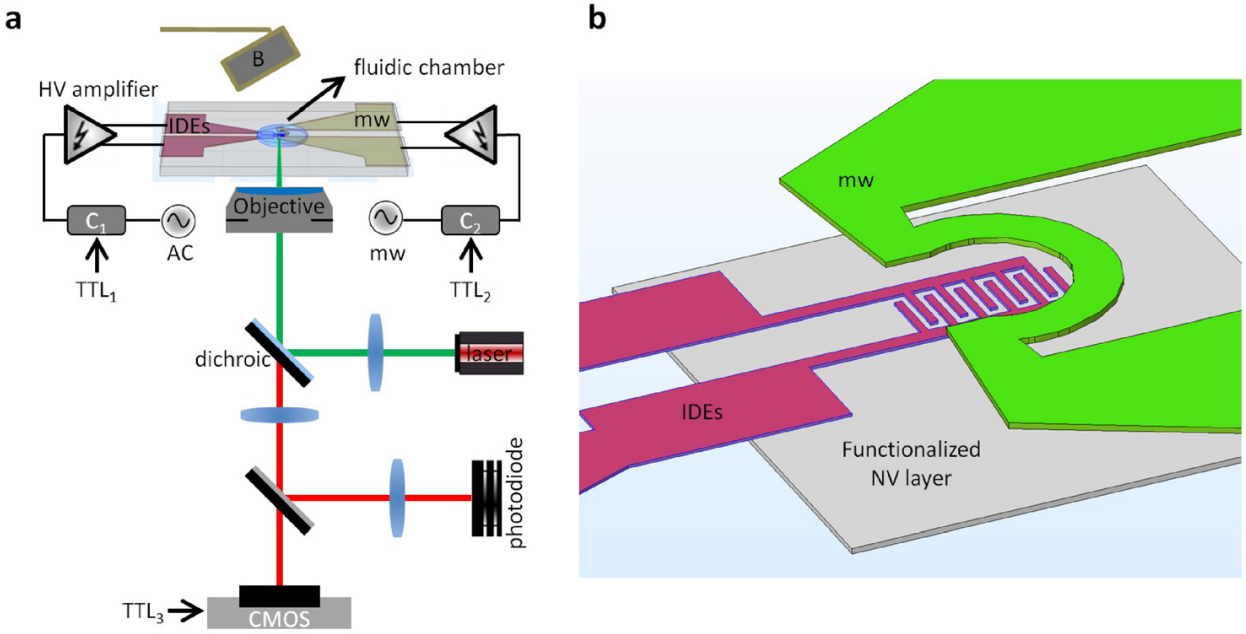

Figure 3.10: (a) DEP-force spectrometer integrated with an NV magnetic imaging setup for the quantitative measurements of non-covalent interactions. The photodiode is used to align the bias magnetic field to one of the crystallographic directions of NV centers in the diamond lattice by observing optically detected magnetic resonance (ODMR). The ODMR spectrum is acquired through optical excitation with a green laser, microwave excitation with a sweeping microwave (mw) generator, and the detection of fluorescence with a CMOS camera. DEP force spectroscopy is performed through the AC signal applied to the inter-digitated microelectrodes (IDEs) integrated on the fluidic chamber. The TTL1 pulse train applied to the switch C1 is for the amplitude modulation of the DEP signal. The TTL2 pulse train applied to the switch C2 and the TTL3 pulse train triggering the CMOS camera are to synchronize the mw source and acquire the fluorescent contrast when the mw is on and off. (b) A close-up of the fluidic chamber indicating the relative axial positioning of the IDEs, mw electrode, and diamond plate with NV centers. The spacings between the functionalized NV layer and IDEs and between the IDEs and the mw electrode are 15 µm and 120 µm, respectively. Reprint from [32], used with permission.

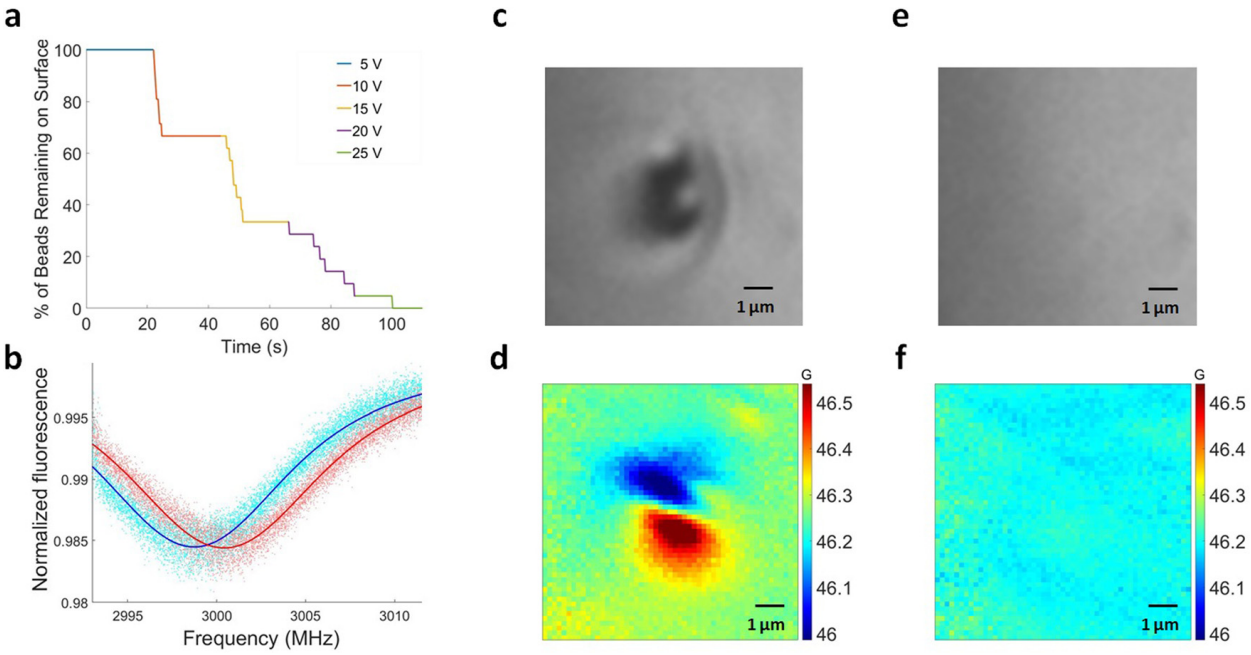

Figure 3.11: (a) Percentage of immovable functionalized magnetic beads as a function of the AC signal amplitude that is applied to the IDEs to generate the DEP force on the beads. Most of the immobilized beads are manipulated when the peak-to-peak voltage is in the range of 10 V to 20 V, which correspond to the 221 pN to 884 pN dielectrophoretic force range. (b) ODMR spectrum of the NV centers reflecting the resonance shifts due to the local magnetic field. Fitted blue and red lines correspond to 46.0 G and 46.5 G, respectively. (c) Bright-field microscopy image of the particle immobilized on the NV layer surface due to the streptavidin-biotin non-covalent interaction. (d) Magnetic image of the same particle acquired through the ODMR spectrum. (e) Bright-field microscopy image after DEP manipulation. (f) Magnetic image of the same area after DEP manipulation. Reprint from [32], used with permission.

the IDEs, demonstrating a useful alternative for future experimentation. A visual summary of the results is shown in Fig. 3.11. A more detailed description of the methods and results described in [32].

3.8 Conclusion

We successfully realized a diamond-based FIRMS experiment capable of both quantifying the strength of the molecular interactions and resolving individual particles using both optical and magnetic imaging. We also developed two separate techniques for manipulating the magnetic microbeads: mechanical oscillations of the chamber via piezo-electric actuators and

dielectrophoretic forces on the particles via electric field gradients. This technique may prove useful in drug testing and diagnostics: we envision a system of multiple parallel microfluidic channels carrying nanoparticles with various functionalizations that are detected with high sensitivity, and whose targeted molecular interaction is quantitatively measured.

Chapter 4

Another application of particle tracking: levitation of a ferromagnetic particle over a superconductor

4.1 A Tangential Analysis

During my time at Berkeley, one of my colleagues, Tao Wang, approached me with an interesting problem. He had obtained video of the levitation of a microscopic magnetic particle, taken while changing the applied magnetic field, and he was interested in characterizing its motion in order to extract information about magnetic properties of the system. In particular, the frequencies of the different modes of motion were believed to be connected to the strength of the applied magnetic field, as well as the flux pinning. The inspiration of the project was a magnetometer based on a compass needle: a frictionless microscopic levitated magnet in a vacuum [33].

The particles used were (Pr,Fe)B ferromagnetic particle with diameter of approximately 25 µm. A single particle is magnetized using a strong permanent magnet and levitated in a niobium well in microscopy cryostat. The pressure in the cryostat is pumped down to a pressure of 1×10^{-5} Pa using a scroll pump and turbo pump. The motion of the levitated particle is described by long-lived oscillations of specific characteristic frequencies. The mechanical motion of the pumps also contribute to the motion of the particle by exciting near-resonant modes, and are thus stopped and disconnected to remove their effect from the motion of the particle.

During levitation, the particle is imaged through a x40 long-working-distance objective (Sunny Lplan40x) onto a CMOS camera (Andor Zyla 5.5 sCMOS), recording video at a framerate of 250 fps. A beam splitter is used to allow for simultaneous imaging and illumination with a microscope illuminator (Thorlabs, Model 21AC) through the back aperture of the objective.

The methods described in this chapter were used and reported on in [34].

4.2 Motion Analysis Techniques

4.2.1 Statistical moments

The first method developed was actually not specific to particles at all, but rather generic motion sensing. If we think about the image as a distribution, and scale the value at each pixel by a constant such that the sum of all pixels is one, we can calculate the first moments of this distribution. These moments give us some sense of a 'center of mass' of the image, and allow us to reduce each image to a pair of coordinates. The main advantage of this technique is that is a extremely efficient, and significantly faster than the other techniques. It also has the advantage of producing results for an arbitrary video file, and does not require and preconceived notion of what the particle should look like. The ability to function even when the particle is absent allows for the possibility of completely separating the particle's motion from the background (Fig. 4.1). However, this technique, unlike the others, is sensitive to noise in all parts in the image, including those far from the particle, and as such was mostly reserved for diagnostic purposes.

4.2.2 Centroid tracking using segmentation

A more conventional method for analyzing the motion of the particle is using segmentation, or the process through which an image is divided into sections. Here, we use thresholding to divide the region into two sections: pixels above a certain value are classified as 'background', and pixels below a certain value are classified as 'particle'. To improve this segmentation, the image was first smoothed with a Gaussian filter, which greatly reduces the noise at high spatial frequencies. The largest contiguous block of 'particle' pixels was identified to be the particle, and all other 'particle' pixels were reclassified as 'background.' Finally, the centroid (center of mass) of the particle was calculated in order to obtain the coordinates of the particle during that particular image.

The main difficulty encountered when performing this method is choosing a suitable value for thresholding. It is important to allow the thresholding value be different for each frame of the video to avoid creating artifacts in the resulting centroid position. If the thresholding value is chosen correctly, then the pixels on the boundary of the segmented region should possess a high gradient, when compared to the rest of the pixels in the image. Taking advantage of this fact, the threshold was varied for each image such that the mean magnitude of the gradient at pixels comprising the boundary was maximized.

This technique was further improved by repeating it a second time, but on an image that has its background subtracted. This is especially important when the background appears to have large gradients near the particle. The first iteration is used to determine which pixels comprise the background. The background is determined by averaging the background pixels among all of the frames in the video file. A small caveat is that if the particle does not significantly move during the video, there will be some pixels that are never part of the background, and therefore a background estimate for those pixels cannot be obtained. This

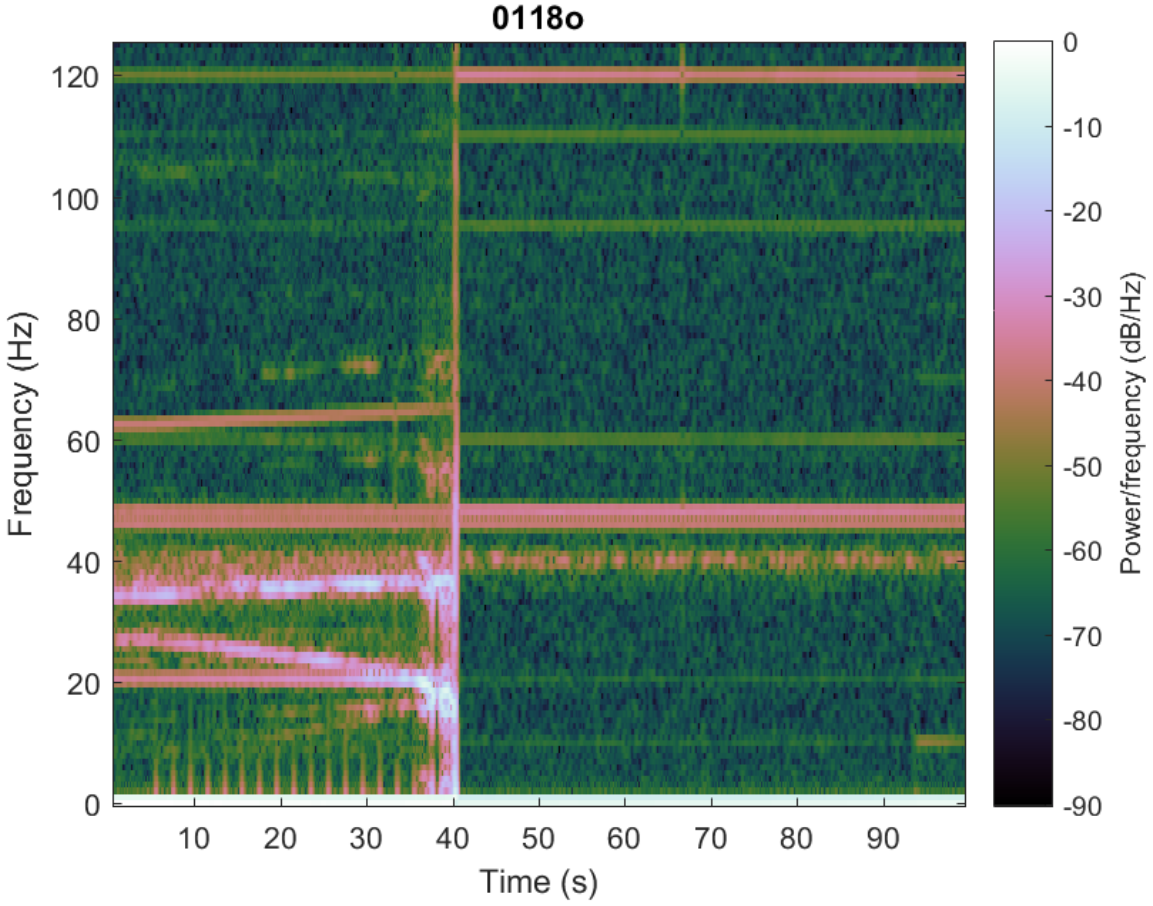

Figure 4.1: Fourier analysis of statistical moments. At around $t = 40\,\mathrm{s}$ the particle was lost, and for the rest of the video only the background was visible. From this image, it is clear which frequencies correspond to motion of the particle, and which correspond to motion of the background. The vertical spikes at frequencies under 5 Hz occurring every 2 s correspond to step-wise increments of the applied magnetic field.

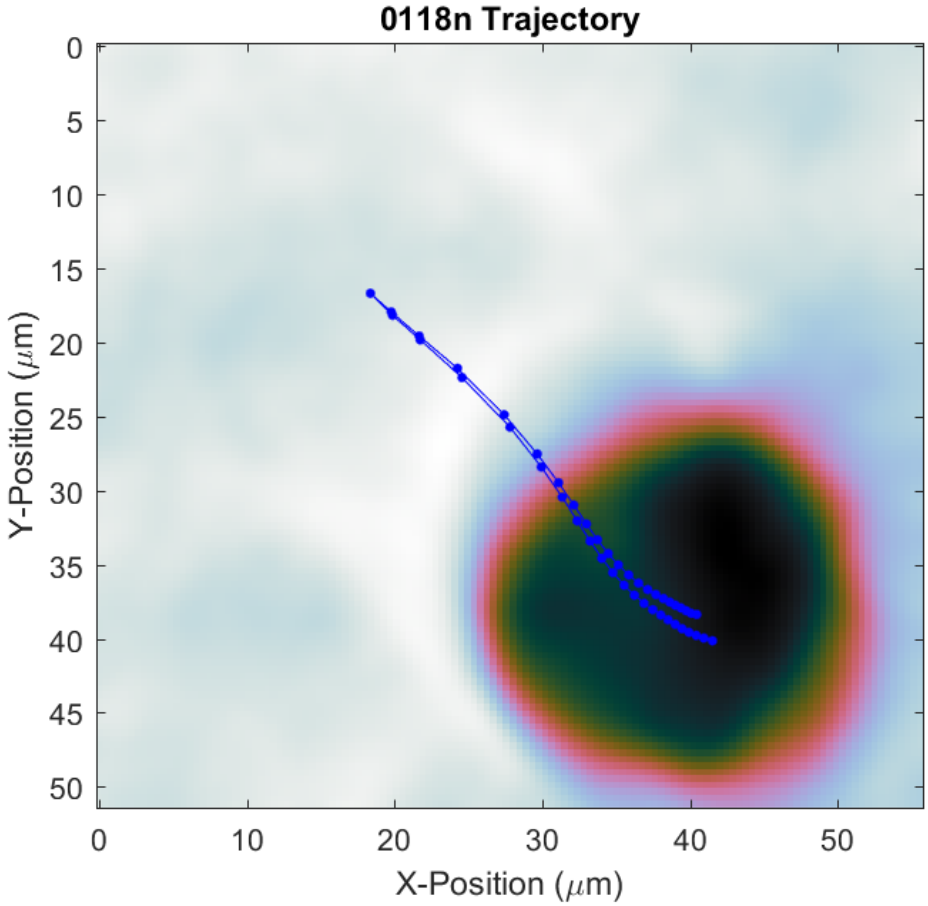

Figure 4.2: Image of the particle after smoothing and background subtraction, with its trajectory throughout the experiment. When the applied magnetic field is ramped up and back down, the particle retraces its path. Reprint from [34], used with permission.

background subtraction improvement was only performed on video files where the particle was observed to move by at least one diameter.

This particle tracking technique compares very favorably to the moment technique in all situations where it succeeds in identifying the particle. Specifically, this technique has a greatly reduced background, since unlike the moment technique, motion in the background of the image does not significantly affect the position of the centroid of the particle. An image of the particle and its trajectory are shown in Fig. 4.2.

4.2.3 Fourier analysis

Both of these techniques, statistical moments and centroid tracking, convert a sequence of images into a sequence of pairs of coordinates. In order to obtain information about the frequencies of the motion, Fourier analysis was performed on the coordinates. Since the Fourier transform acts on a set of complex numbers, to simplify the analysis, the pairs of coordinates were converted into a 1-D array of complex numbers.

In order to obtain frequency information of the motion of the particle as a function of time, a spectrogram was generated using the position data. Spectrograms are obtained by calculating the Fourier transform for different time windows of the data. Larger windows produce Fourier transforms with higher resolution, but result in fewer windows, meaning lower time resolution. Because the applied magnetic field was incremented in steps, these windows were chosen to be the periods of time when the applied magnetic field was constant.

When converting our complex-valued Fourier transform into magnitudes to be plotted in a spectrogram, we have actually lost some valuable information that was stored in the phase. Each pixel in the spectrogram only displays a magnitude, but before taking the magnitude, each pixel contains a real and imaginary part. Furthermore, the Fourier transfer of a complex-valued function produces an asymmetric spectrum around zero, so there are different values at $\pm f_0$. The upshot is that each pixel in the spectrogram has 4 corresponding (real) values that have been combined into a single magnitude, and these 4 values can also be combined to obtain the angle of the oscillations.

To more clearly illustrate this concept, imagine a particle moving in the x-y plane with motion only at the angular frequency ω_0. A general form of this motion can be described by the following equations:

$$x(t) = (A + C)\cos\omega_0 t + (D - B)\sin\omega_0 t, \tag{4.1}$$

$$y(t) = (D + B)\cos\omega_0 t + (A - C)\sin\omega_0 t, \tag{4.2}$$

$$\begin{aligned} z(t) &= x(t) + iy(t) \\ &= (A + iB)\, e^{i\omega_0 t} + (C + iD)\, e^{-i\omega_0 t}. \end{aligned} \tag{4.3}$$

Here we have defined $z(t)$ to be the complex representation of both horizontal and vertical motion. A and B can be thought of as encoding the magnitude and phase of a counter-clockwise rotation of the particle. Similarly, C and D can be thought of as encoding the magnitude and phase of a clockwise rotation of the particle. After taking the Fourier transform of $z(t)$ we can directly obtain the values A, B, C, and D from the frequencies $\omega = \pm\omega_0$:

$$Z(\omega) = \int_{-\infty}^{\infty} z(t) e^{-i\omega t} dt, \tag{4.4}$$

$$Z(\omega) = (A + iB)\,\delta(\omega - \omega_0) + (C + iD)\,\delta(\omega + \omega_0). \tag{4.5}$$

Generally, $x(t)$ and $y(t)$ describe an ellipse, which has values for semi-major axis (r_{max}),

semi-minor axis (r_{min}), and angle between major axis and x-axis (ϕ).

$$r_{max} = \left(A^2 + B^2 + C^2 + D^2 + 2\sqrt{A^2C^2 + A^2D^2 + B^2C^2 + B^2D^2}\right)^{\frac{1}{2}} \tag{4.6}$$

$$r_{min} = \left(A^2 + B^2 + C^2 + D^2 - 2\sqrt{A^2C^2 + A^2D^2 + B^2C^2 + B^2D^2}\right)^{\frac{1}{2}} \tag{4.7}$$

$$\phi = \frac{1}{2}\,\mathrm{atan2}(AD - BC, AC + BD). \tag{4.8}$$

The fourth independent quantity that can be extracted from the values A, B, C, and D is the global phase of the oscillation, which contains no physically meaningful information about our system.

The proper way to combine these values to obtain the power in a specific frequency band at a particular time is to add the perpendicular amplitudes in quadrature.

$$\begin{aligned} r &= \sqrt{r_{max}^2 + r_{min}^2} \\ &= \sqrt{A^2 + B^2 + C^2 + D^2} \end{aligned} \tag{4.9}$$

In addition to finding a value for r, for each frequency and time, we can also obtain a value of ϕ for each frequency and time. The value for ϕ becomes very noisy where the value for r is small, so to more easily visualize this data, images were generated with a white or black background, where the transparency of the image depends on r, and the color of the image depends on ϕ, shown in (Fig. 4.3).

4.2.4 Correlations

The final and most generally applicable method for analyzing period motion involves an analysis of the correlations between images. One major drawback of the previous methods is that it is possible that the coordinates of the centroid, as well as the first moments of the image, are insensitive to the rotation of the object. By measuring correlations, the periodic nature of any kind of motion can be detected. This method was developed by adapting techniques described in Ref. [35], where the videos depict moving people and vehicles, taken primarily from aerial footage.

This process consists of correlating the ith frame with the jth frame in order to create an $N \times N$ similarity matrix, which can be displayed as an image. Any periodicity in the motion will produce corresponding diagonal lines, parallel to the line of $i = j$, with spacing corresponding to the period of motion. Taking the power spectrum of the i'th row will reveal the prominent frequency components present in the motion at that particular time. The power spectra of all of the rows can be combined into a single image to form a spectrogram, similar to the results of the techniques previously discussed. Spectrograms generated for the same data set using both centroid tracking and correlation analysis techniques are shown in Fig. 4.4.

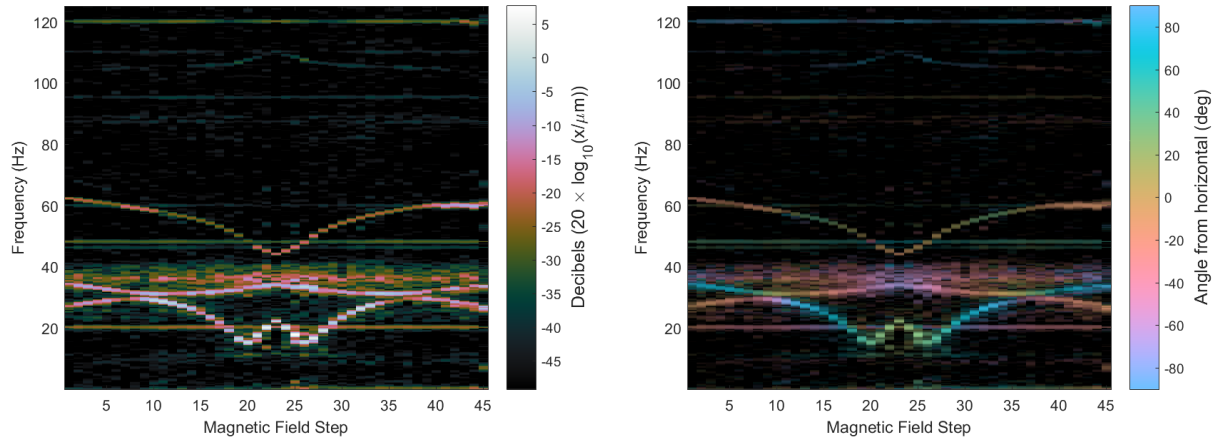

Figure 4.3: (Left) A conventional spectrogram. (Right) A spectrogram where the angle of the motion is encoded as the color of each pixel. The angle of the motion is observed to change as the magnetic field is increased and decreased.

There are several ways one could go about obtaining a correlation value between frames. Rather than detecting motion by measuring a change in pixel value, correlation values were obtained by measuring a change in classification of each pixel. This was done using the using the segmentation results obtained from the centroid tracking method, which were observed to very accurately identify which pixels comprised the particle. The correlation value was calculated by dividing number of the pixels classified to be 'particle' in both images by the number of pixels classified to be 'particle' in at least one image.

In order to reduce the time required to compute the similarity matrix, only 500 elements for each row, starting from the diagonal, were computed. Even so, the computation time was prohibitive, and the analysis was only performed on a few video files.

4.3 Conclusion

While each method has its advantage, overall, the most useful method for analyzing the motion of the particle is the centroid tracking method. This should not come as a surprise, since the other methods are very general methods that work to detect any kind of motion, while the centroid tracking is specific to our specific problem.

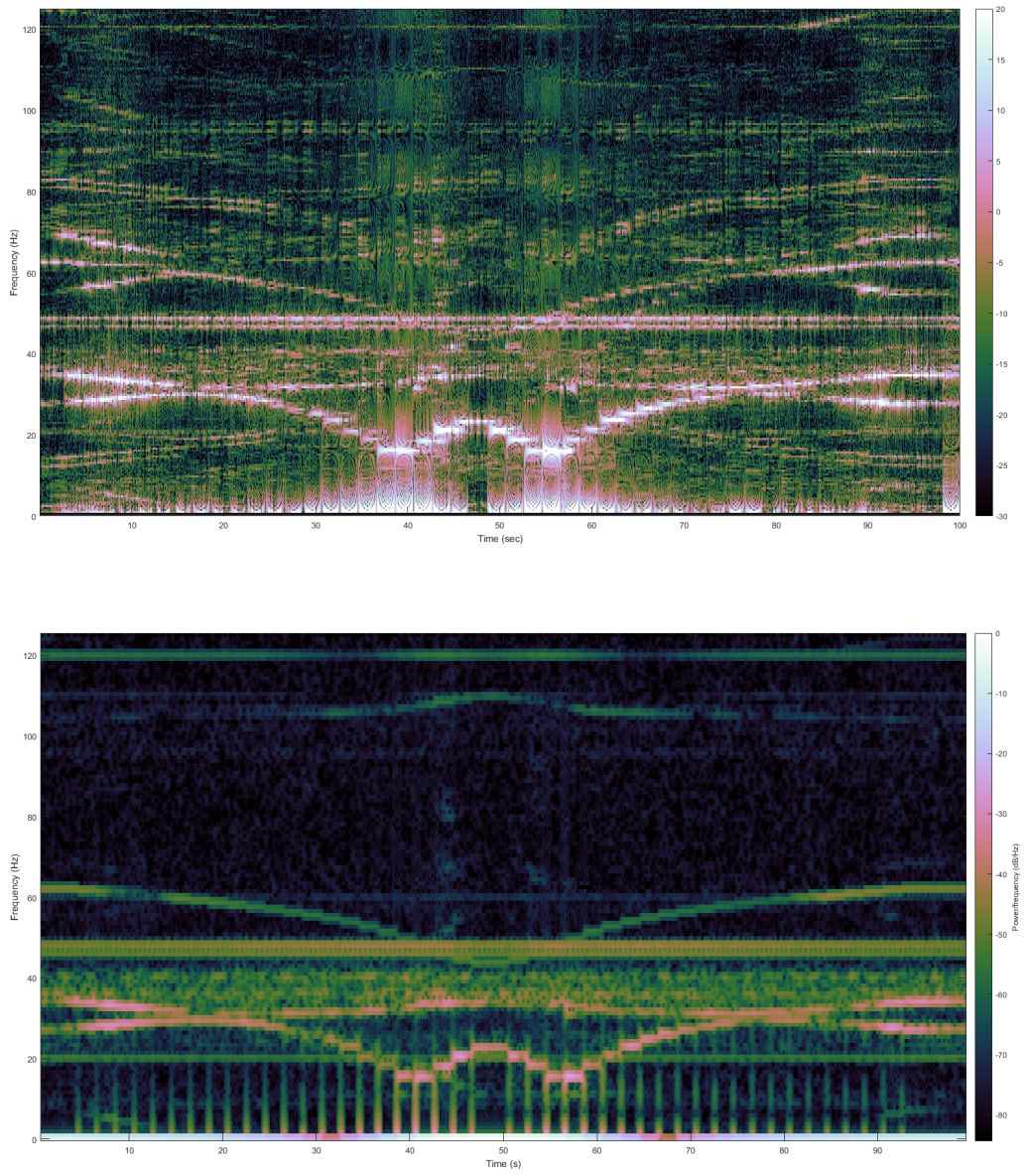

Figure 4.4: The analysis of a particles motion using (Top) correlations between frames and (Bottom) tracking of the centroid. The correlation method reveals some additional lines not visible when using the centroid method.

Chapter 5

Conclusions and Outlook

In this dissertation, a brief introduction to the physics of NV centers was provided, with a focus on magnetometry using ensembles of NV centers. The operating principles and experimental details of an NV-based imaging magnetometer were then discussed. Next, a specific application of NV-based magnetic imaging was described, one in which biomolecular noncovalent bonds were labelled with magnetic microbeads and whose interaction strengths were measured. Finally, in a somewhat unrelated experiment sharing the similarities of both magnetometry and imaging of the tracking of microparticles, the methods used to analyze the motion of a levitated particle in order to extract frequency information were described.

In future work, a direction for FIRMS that would be worth exploring is utilizing flow, with microfluidics. This can help overcome the main limitation of the chambers: a lack of reusability. A microfluidic chamber could provide hundreds of experimental cycles compared to a single experiment for a sealed chamber, and with reproducibility would come improved force sensitivity. Another possible direction would be to perform FIRMS with smaller particles, allowing for a greater number of particles covering a similar surface area. Using smaller particles however, would reduce the force applied through either piezoelectric actuators or dielectrophoresis, as both methods produce smaller forces on smaller particles. This may not pose a problem for dielectrophoresis, where detaching 2 µm diameter beads could be done with ease for particles nearest to the IDEs.

Bibliography

[1] A.M. Zaitsev. *Optical Properties of Diamond. A Data Handbook*. Springer, 2001.

[2] Igor Aharonovich, Andrew Greentree, and S. Prawer. "Diamond photonics". In: *Nature Photonics - NAT PHOTONICS* 5 (June 2011), pp. 397–405. DOI: 10.1038/nphoton.2011.54.

[3] Jeronimo Maze et al. "Properties of nitrogen-vacancy centers in diamond: The group theoretic approach". In: *New Journal of Physics* 13 (Oct. 2010). DOI: 10.1088/1367-2630/13/2/025025.

[4] A. Lenef and S. C. Rand. "Electronic structure of the N-V center in diamond: Theory". In: *Phys. Rev. B* 53 (20 May 1996), pp. 13441–13455. DOI: 10.1103/PhysRevB.53.13441.

[5] M. W. Doherty et al. "Theory of the ground-state spin of the NV^- center in diamond". In: *Phys. Rev. B* 85 (20 May 2012), p. 205203. DOI: 10.1103/PhysRevB.85.205203.

[6] V. M. Acosta et al. "Optical properties of the nitrogen-vacancy singlet levels in diamond". In: *Phys. Rev. B* 82 (20 Nov. 2010), p. 201202. DOI: 10.1103/PhysRevB.82.201202.

[7] Victor Acosta. "Optical Magnetometry with Nitrogen-Vacancy Centers in Diamond". PhD thesis. University of California, Berkeley, 2011.

[8] Marcus Doherty et al. "The nitrogen-vacancy colour centre in diamond". In: *Physics Reports* 528 (Feb. 2013). DOI: 10.1016/j.physrep.2013.02.001.

[9] Kasper Jensen, Pauli Kehayias, and Dmitry Budker. "Magnetometry with Nitrogen-Vacancy Centers in Diamond". In: vol. 19. Sept. 2017, pp. 553–576. ISBN: 978-3-319-34068-5. DOI: 10.1007/978-3-319-34070-8_18.

[10] Peter Woit. *Quantum Theory, Groups and Representations. An Introduction*. Springer, 2017.

[11] Jacob Taylor et al. "High-sensitivity diamond magnetometer with nanoscale resolution". In: *Nature Physics* 7 (May 2008). DOI: 10.1038/nphys1075.

[12] Nir Bar-Gill et al. "Solid-state electronic spin coherence time approaching one second". In: *Nature communications* 4 (Apr. 2013), p. 1743. DOI: 10.1038/ncomms2771.

[13] Jeronimo Maze et al. "Nanoscale magnetic sensing with an individual electronic spin in diamond". In: *Nature* 455 (Nov. 2008), pp. 644–7. DOI: 10.1038/nature07279.

[14] Thomas Wolf, Philipp Neumann, and Junichi Isoya. "Subpicotesla Diamond Magnetometry". In: *http://arxiv.org/abs/1411.6553* (Nov. 2014). DOI: 10.1103/PhysRevX.5.041001.

[15] Ilja Fescenko et al. "Diamond Magnetic Microscopy of Malarial Hemozoin Nanocrystals". In: *Physical Review Applied* 11 (Mar. 2019). DOI: 10.1103/PhysRevApplied.11.034029.

[16] S. B. van Dam et al. "Optical coherence of diamond nitrogen-vacancy centers formed by ion implantation and annealing". In: *Phys. Rev. B* 99 (16 Apr. 2019), p. 161203. DOI: 10.1103/PhysRevB.99.161203.

[17] S. Lourette et al. "Noncovalent force spectroscopy using wide-field optical and diamond-based magnetic imaging". In: *Journal of Applied Physics* 126 (Nov. 2019), p. 194502. DOI: 10.1063/1.5125273.

[18] Lashan De Silva et al. "Well-Defined and Sequence-Specific Noncovalent Binding Forces of DNA". In: *The Journal of Physical Chemistry B* 117.25 (2013), pp. 7554–7558. DOI: 10.1021/jp403817b.

[19] Haina Jia, Yuhong Wang, and Shoujun Xu. "Super-resolution force spectroscopy reveals ribosomal motion at sub-nucleotide steps". In: *Chem. Commun.* 54 (46 2018), pp. 5883–5886. DOI: 10.1039/C8CC02658K.

[20] Taisuke Ota, Tadao Sugiura, and Satoshi Kawata. "Rupture force measurement of biotin-streptavidin bonds using optical trapping". In: *Applied Physics Letters* 87.4 (2005), p. 043901. DOI: 10.1063/1.1999855.

[21] Stanislaus S. Wong et al. "Covalently functionalized nanotubes as nanometresized probes in chemistry and biology". In: *Nature* 394.6688 (July 1998), pp. 52–55. ISSN: 0028-0836. DOI: 10.1038/27873.

[22] Joyce Wong, Ashutosh Chilkoti, and Vincent T Moy. "Direct force measurements of the streptavidin–biotin interaction". In: *Biomolecular Engineering* 16.1 (1999), pp. 45–55. ISSN: 1389-0344. DOI: 10.1016/S1050-3862(99)00035-2.

[23] Anke Krueger et al. "Biotinylated Nanodiamond: Simple and Efficient Functionalization of Detonation Diamond". In: *Langmuir* 24.8 (2008), pp. 4200–4204. DOI: 10.1021/la703482v.

[24] E. Hecht. *Optics*. Pearson education. Addison-Wesley, 2002, pp. 291–302.

[25] R Merkel et al. "Energy landscapes of receptor-ligand bonds explored with dynamic force spectroscopy". In: *Nature* 397 (6714 Jan. 1999), pp. 50–53. DOI: 10.1038/16219.

[26] Evan A. Evans and Ken Ritchie. "Dynamic strength of molecular adhesion bonds." In: *Biophysical journal* 72 (4 1997), pp. 1541–55. DOI: 10.1016/S0006-3495(97)78802-7.

[27] Li Yao and Shoujun Xu. "Force-Induced Remnant Magnetization Spectroscopy for Specific Magnetic Imaging of Molecules". In: *Angew. Chem. Int. Ed.* 50.19 (2011), pp. 4407–4409. DOI: 10.1002/anie.201007297.

[28] Herbert Ackland Pohl. "Dielectrophoresis". In: *The behavior of neutral matter in nonuniform electric fields* (1978).

[29] C M Feeley and H A Pohl. "The influence of resistivity and permittivity on the motion of uncharged solid particles in non-uniform electric fields (the dielectrophoretic effect)". In: *Journal of Physics D: Applied Physics* 14.11 (Nov. 1981), pp. 2129–2138. DOI: 10.1088/0022-3727/14/11/020.

[30] Thomas B. Jones. *Electromechanics of Particles*. Cambridge University Press, 1995. DOI: 10.1017/CBO9780511574498.

[31] "The Clausius-Mossotti Factor". In: *Dielectrophoresis*. John Wiley & Sons, Ltd, 2017. Chap. 6, pp. 119–144. ISBN: 9781118671443. DOI: 10.1002/9781118671443.ch6.

[32] Metin Kayci et al. "Quantitative measurements of non-covalent interactions with diamond based magnetic imaging". In: *Applied Physics Letters* 113.5 (2018), p. 053103. DOI: 10.1063/1.5041513.

[33] Derek F. Jackson Kimball, Alexander O. Sushkov, and Dmitry Budker. "Precessing Ferromagnetic Needle Magnetometer". In: *Phys. Rev. Lett.* 116 (19 May 2016), p. 190801. DOI: 10.1103/PhysRevLett.116.190801.

[34] Tao Wang et al. "Dynamics of a Ferromagnetic Particle Levitated over a Superconductor". In: *Physical Review Applied* 11 (Apr. 2019). DOI: 10.1103/PhysRevApplied.11.044041.

[35] Ross Cutler and Larry Davis. "Real-time periodic motion detection, analysis, and applications". In: *IEEE Trans. Patt. Anal. Mach. Intell* 2 (Feb. 1999), 332 Vol. 2. DOI: 10.1109/CVPR.1999.784652.